ELSEVIER

Contents lists available at ScienceDirect

Remote Sensing of Environment

journal homepage: www.elsevier.com/locate/rse





Novel algorithms for pair and pixel selection and atmospheric error correction in multitemporal InSAR

Jui-Chi Lee *, Manoochehr Shirzaei

Department of Geosciences, Virginia Polytechnic Institute and State University, Blacksburg, VA, USA

ARTICLE INFO

Edited by Jing M. Chen

Keywords: SBAS Sentinel-1 Atmospheric delay InSAR time series Pair selection Pixel selection Smooth 2D splines Delaunay triangulation

ABSTRACT

Entering the SAR's golden era began with the launch of Sentinel-1A/B satellites in 2014 and 2016 with 6-12 day revisit time, much larger stacks of high-resolution SAR images are available over a given area to perform time series analysis. Algorithms that deal with large stack sizes face several challenges, including interferometric phase quality degradation due to signal decorrelations, phase closure error caused by applied multilooking, and tropospheric phase delay. Here, we present an improved SBAS-type algorithm suitable for processing a large stack of SAR images at an arbitrary resolution. We develop a new pair selection strategy that applies dyadic downsampling combined with widely used Delaunay Triangulation to identify an optimal set of interferometric pairs that minimize systematic errors due to short-lived signals and closure errors. We develop and apply a novel statistical framework that selects elite pixels accounting for distributed and permanent scatterers. Also, we implement a new tropospheric error correction that takes advantage of smooth 2D splines to identify and remove error components with fractal-like structures. We demonstrate the effectiveness of the algorithms by applying them to 3 large datasets of Sentinel-1 SAR images measuring non-linear surface deformation over various terrains. Compared with independent GNSS observations, we find that over the rural/natural terrains adjacent to San Andreas fault in southern California, our approach yields a standard deviation of 0.48 cm for time series differences in both ascending and descending tracks. While in urban areas, such as Los Angeles, standard deviation difference with GNSS time series is 0.30 cm.

1. Introduction

Interferometric Synthetic Aperture Radar (InSAR) is an efficient tool to measure mm-level land surface deformation at a regional scale and high resolution (Burgmann et al., 2000; Franceschetti and Lanari, 1999; Hanssen, 2001; Massonnet and Feigl, 1998; Rosen et al., 2000). The availability of high temporal resolution time series of SAR acquisitions from various missions, such as Sentinel-1 and the upcoming NASA-India Synthetic Aperture Radar (NISAR), enables measuring the time-history of land surface deformation with a temporal sampling rate of a few days. Currently, two main classes of time series algorithms are implemented, including Small BAseline Subset (SBAS) (Berardino et al., 2002; Schmidt and Bürgmann, 2003) and Persistent Scatterers Interferometry (PSI) (Ferretti et al., 2001; Hooper et al., 2007). SBAS and PSI algorithms refer to different strategies of combining SAR images following coregistration to a reference image. Given n coregistered SAR images, PSI generates only n-1 interferograms, while SBAS may generate up to nC2 = n!/2!(n-2)!, (C is a combination operator). Both approaches include a procedure for identifying elite pixels that carry high-quality phase measurements. However, depending on the study area, each may have some advantages, as the targeted pixels are different. SBAS forms interferograms of short temporal and perpendicular baseline and identifies distributed scatterers (DS) with moderate to high coherence in most interferograms. In contrast, PSI identifies Permanent Scatterers (PS), namely pixels with stable phase values throughout the observation period, primarily associated with artificial structures. However, the number of permanent scatterers in rural areas and natural terrain is minimal. As a result, some studies tried to combine PS and DS to increase elite pixel density (Ferretti et al., 2011; Hooper, 2008). An advantage of the SBAS algorithm is its ability to take advantage of redundant observations, enabling adjusting errors and identifying outliers caused by improper phase unwrapping. However, both approaches can yield comparable land surface deformation rates and time series results (Shanker et al., 2011). Furthermore, both PSI and SBAS approaches apply a suite of corrections to reduce environmental artifacts, particularly the tropospheric delay. Currently, there are two main classes of

E-mail address: vickielee@vt.edu (J.-C. Lee).

^{*} Corresponding author.

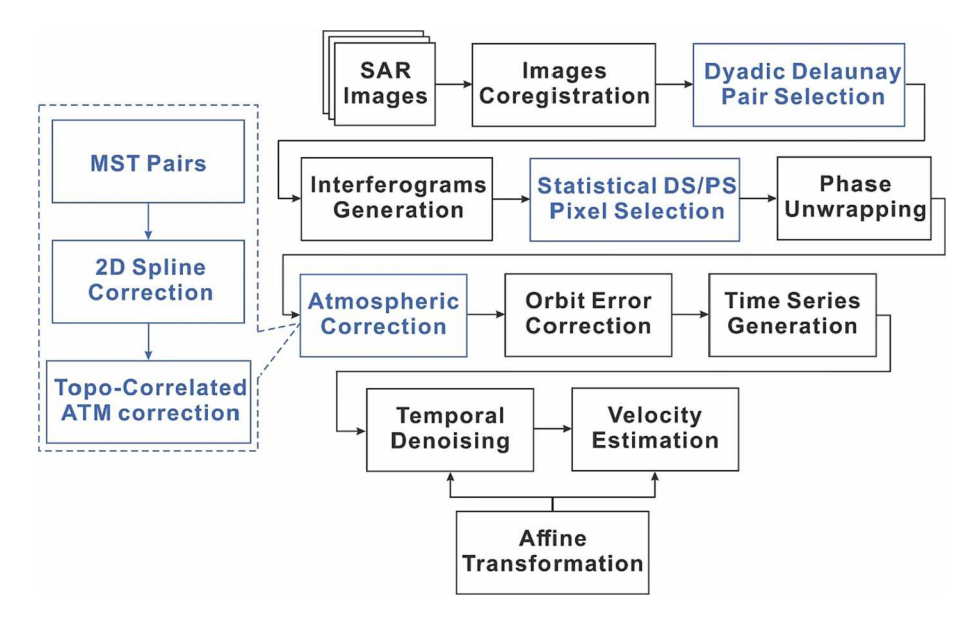


Fig. 1. Processing flowchart. Boxes highlighted in blue include this work contribution. MST: Minimum Spanning Tree; Topo-Correlated ATM Correction: Topographic-Corrected Atmospheric Correction. (For interpretation of the references to colour in this figure legend, the reader is referred to the web version of this article.)

correction approaches: model-based and filter-based. In model-based correction, numerical weather model (e.g., (Y. Cao et al., 2021; Dee et al., 2011; Eff-Darwich et al., 2012; Foster et al., 2006, 2013; Puysségur et al., 2007; Wadge et al., 2010; Webley et al., 2004)) informed by data from satellite spectrometers, such as MODIS or MERIS (e.g., (Li et al., 2005, 2006, 2009; Walters et al., 2013)) and Global Navigation Satellite System (GNSS) observation are often used (e.g., (Löfgren et al., 2010; Onn and Zebker, 2006; Yu et al., 2017, 2018)). Overall, these approaches yield promising results, but some studies reported mixed results that sometimes the correction model did not perform well (e.g., (Y. Cao et al., 2021; Foster et al., 2013; Hobiger et al., 2010; Samsonov et al., 2014)). On the other hand, the filter-based correction methods apply a spatial-temporal smoothing operator (Berardino et al., 2002; Ferretti et al., 2001), and explore relationships between the stratified tropospheric delay and topographic height (e.g., (Bekaert et al., 2015; Doin et al., 2009; Lin et al., 2010; Shirzaei and Bürgmann, 2012)), or a combination of them. The SAR community entered a new era when Sentinel-1A/B C-Band satellites of the European Space Agency were launched in 2014 and 2015. Thanks to the mission's 6-12 day revisit time, short data latency, and open-data policy, much larger stacks of SAR datasets are available over a given area to perform time series analysis. Although the conventional InSAR time series methods proved effective in analyzing a stack of Sentinel-1 datasets (Shirzaei et al., 2017), some problems have also emerged in dealing with such temporally and spatially high-resolution observations. For instance, (Ansari et al., 2020) pointed out that only using short temporal baseline multi-looked interferograms for SBAS analysis may result in a systematic error affecting estimated land surface deformation, which is associated with the short-lived signals (de Zan et al., 2014, 2015; de Zan and Gomba, 2018). With larger stacks of data, signal decorrelation might also impact the accuracy. (Michaelides et al., 2019) propose a method using singular value decomposition, and (Zhang et al., 2019) use the least absolute shrinkage and selection operator to estimate the decorrelation phase. Here, we propose an improved SBAS-type algorithm optimized for processing high spatiotemporal resolution SAR datasets. We develop a new pair selection strategy that allows selecting m < < nC2 interferograms yet avoids systematic errors due to shortlived signals. We further develop a novel pixel selection algorithm that accounts for both DS and PS pixels. Also, we implement a new atmospheric correction that takes advantage of smooth 2D splines. We demonstrate the effectiveness of the algorithms by applying them to 3 large SAR datasets acquired by Sentinel-1 satellites over natural and urban terrains in southern California to measure non-linear surface deformation. We use independent observation of the Global Navigation Satellite System (GNSS) to validate our results.

2. Method

Our algorithm improves an existing multitemporal approach, Wavelet-Based InSAR time series (WabInSAR) after (Shirzaei et al., 2019; Shirzaei and Bürgmann, 2012, 2013), but can be easily integrated into other InSAR time series algorithms. Fig. 1 presents the flowchart of the processing algorithm we implemented in this study. Assuming n Sentinel-1 SAR images are taken from a similar viewing geometry over the area of interest, we begin with coregistering images to a reference one and generate SAR images. We implement a matching algorithm that uses precise orbital ephemeris, a digital elevation model (DEM), and amplitude images to align all images to a single reference (Sansosti et al., 2006). We further apply an enhanced spectral diversity (ESD) approach to achieving a coregistration accuracy of 0.001 pixels to minimize the phase error in the azimuth direction (Shirzaei et al., 2017; Yague-Martinez et al., 2016). Next, we generate m pairs following the approach described in section 2.1, which minimizes the computation time, reduces phase closure errors (Michaelides et al., 2019), and avoids systematic errors caused by using only short baseline interferograms (Ansari et al., 2020) and minimizes the phase temporal decorrelation. In the following, we develop and apply a new framework (section 2.2) that assesses the statistical similarity between DS and PS amplitudes history and generates an ensemble comprising PS and most similar DS pixels. Next, we apply a 2D sparse phase unwrapping algorithm using a minimum cost-flow algorithm (Costantini and Rosen, 1999) to estimate absolute phase values for each elite pixel (Costantini, 1998). We correct each unwrapped interferogram for the effect of atmospheric delay using the approach discussed in section 2.3. As an optional step, we identify and remove the long-wavelength signal in the spatial domain, possibly due to ionospheric delay or residual orbital error following (Shirzaei and Walter, 2011). The residual orbital error in Sentinel-1 is negligible, particularly when using precise ephemeris data (Shirzei et al. 2017). Also, ionospheric errors can be corrected using different techniques (e. g., Zhang et al. (2022)). Next, we apply a re-weighted least-squares to

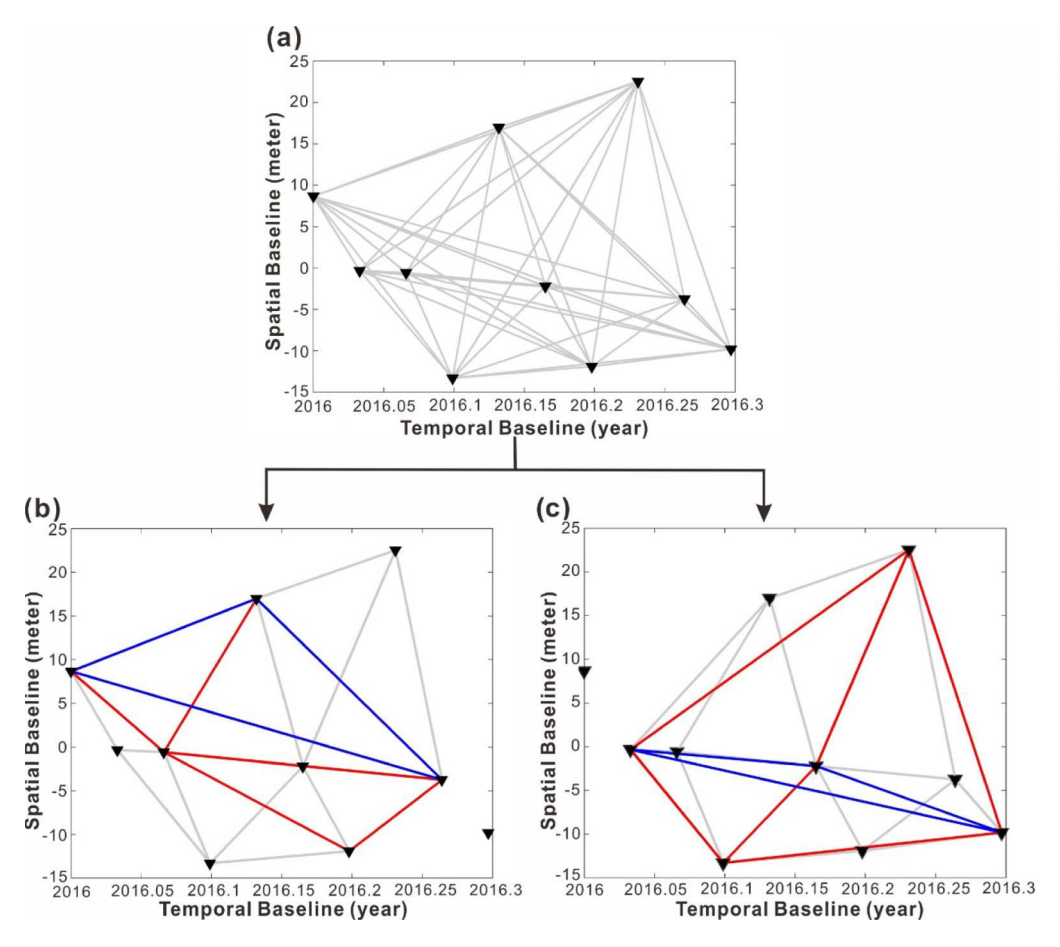


Fig. 2. Synthetic scenarios, including a dataset of 10 SAR images and Dyadic Delaunay Triangulation used for pair selection. Black-filled triangles are the SAR scenes. (a) Gray lines are all the possible pairs, (b, c) Sets S1 and S2. Gray lines are the triplets before downsampling comprising short baseline pairs, red lines are the triplets after the first round of dyadic downsampling, and blue lines are triplets after the second round of downsampling. (For interpretation of the references to colour in this figure legend, the reader is referred to the web version of this article.)

estimate the phase change time series for each elite pixel (Shirzaei and Bürgmann, 2013). The phase measurement weight matrix is considered proportional to the interferometric phase coherence. We apply a highpass filter based on continuous wavelet transforms to reduce the atmospheric delay's temporal component in the elite pixel's surface deformation time series (Shirzaei and Bürgmann, 2013). An optional step to further smooth the signal in time is applying a triangular, rectangular or Gaussian filter to each time series (e.g. (Berardino et al., 2002; Ferretti et al., 2001)). The linear velocities are obtained as the slope of the best-fitting line using a minimum cost-flow algorithm (Costantini and Rosen, 1999).

2.1. Pair selection

Delaunay Triangulation is widely used in SBAS-type algorithms (e.g., (Pepe, 2009; Pepe and Lanari, 2006)) to generate a set of interferometric pairs. Here, we implement an iterative algorithm that combines Dyadic Downsampling and Delaunay Triangulation, as sketched in Fig. 2. We aim to devise a selection strategy that exploits all available images and yields a set of pairs with a roughly similar number of pairs with different temporal baselines to achieve an adequate signal-to-noise ratio for surface deformation and limit the phase temporal decorrelation. Assuming n SAR images, we divide the dataset into two subsets of $S^1 = \{1, 2, ..., n\}$ - 1) and $S^2 = \{2,3,...,n\}$, comprising n_1^1 and n_2^2 SAR images. We generate k_1^1 and k_1^2 triplets, including all possible unique pairs (i.e., n_1^1 C2 and n_1^2 C2) of P_1^1 and P_1^2 , given temporal and spatial baselines shorter than a threshold to minimize the decorrelation errors. Next, we iteratively downsample each subset by a factor of 2. In interaction i, n_i^1 and n_i^2 are number of SAR images, k_i^1 and k_i^2 are the number of triplets, and P_i^1 and P_i^2 are the number of pairs. The down-sampling repeats for I iterations until each set is left with <3 images. The final set of m unique pairs is

$$P = \left\{ \sum_{i}^{I} P_{i}^{1} \cup P_{i}^{2} - \sum_{i}^{I} P_{i}^{1} \cap P_{i}^{2} \right\}$$
 (1)

where \bigcup . and \bigcap . are union and intersection operators. The set *P* comprises *m* pairs that have a variable temporal baseline (smaller than a threshold) and allow adjusting the closure phase ξ defined as

$$\xi_{abc} = \delta\phi_{ab} + \delta\phi_{bc} - \delta\phi_{ac} \tag{2}$$

where $\delta\phi_{jk}$ is the interferometric phase measured between times t_j and t_k , and a, b and c are three epochs of images forming a triplet. To assess the robustness of the presented pair selection strategy, we perform a variance-covariance analysis of the unknown phase vector $\phi = [\phi(t_1), \phi(t_2), ..., \phi(t_n)]$. Given interferometric phase $\delta\phi^T = [\delta\phi_1, \delta\phi_2, ..., \delta\phi_m]$ measured by m interferograms, the following stochastic relation exists (Mikhail, 1976):

$$A\phi = \delta\phi + v \tag{3}$$

where v is a normally distributed vector of length $m \times 1$ including the additive noise and A is $m \times n$ matrix as follows:

$$\mathbf{A} = \begin{bmatrix} 0 & 1 & -1 & 0 & \dots \\ 0 & 1 & -1 & 0 & \dots \\ 0 & 0 & 1 & -1 & \dots \\ \dots & \dots & \dots & \dots \end{bmatrix}$$
 (4)

Matrix A is not full rank and to overcome the deficiency, we assume $\phi(t_1) = 0$, which eliminates the first column of matrix A. The solution to an overdetermined system of Eq. (3) is given by:

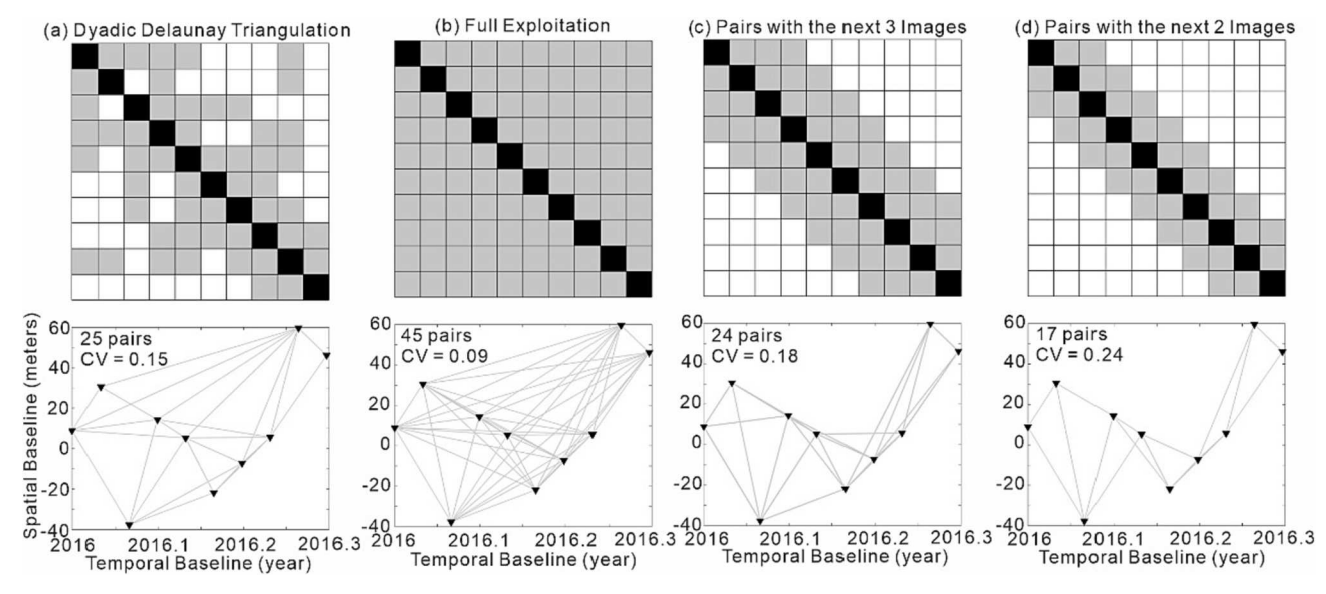


Fig. 3. Different pair selection strategies with the associated coefficient of variation (CV). (a) Considering interferograms produced following our strategy using Dyadic Delaunay Triangulation algorithm, (b) Considering all possible interferograms, (c) Considering only interferograms created by using the following 3 images (Zhang et al., 2019), (d) Considering only interferograms created by using the following 2 images (Zhang et al., 2019).

$$\phi = (A^T W A)^{-1} A^T W \delta \phi \tag{5}$$

$$C_{\phi} = \left(A^{T} W A\right)^{-1} \tag{6}$$

$$CV = std(diag(C_{\phi}))/_{mean(diag(C_{\phi}))}$$
(7)

where \mathbf{W} is $m \times m$ weight matrix, \mathbf{C}_{ϕ} is the $n-1 \times n-1$ variance-covariance matrix, CV is the coefficient of variation, std and mean are standard deviation, mean value and diag is an operator that returns a vector of diagonal components of a square matrix. In practice, the above solution is influenced by the phase decorrelation noise associated with the spatial and temporal baseline length. Pairs of longer baselines have larger decorrelation noise (Pepe, 2009) and thus should be assigned a lower weight. Assuming a constant thermal noise for all the interferometric pairs, we define a theoretical weight matrix as

$$W = I - (\rho_s \cdot \rho_t) \tag{8}$$

where I is the identity matrix and ρ_s and ρ_t are $m \times m$ matrixes of spatial and temporal decorrelation with zero off-diagonal components. The spatial and temporal decorrelation of pair q (i.e., qth diagonal component) are modeled as follows (Zebker and Villasenor, 1992):

$$\rho_s^q = 1 - \frac{2|B_q|R_y cos^2 \theta}{\lambda r} \tag{9}$$

$$\rho_{t}^{q} = exp \left\{ -\frac{1}{2} \left(\frac{4\pi}{\lambda} \right)^{2} \left(d_{y}^{2} sin^{2}\theta + d_{z}^{2} cos^{2}\theta \right) \right\}$$
 (10)

$$d_{\mathbf{v}} = T_{\mathbf{q}} * \mathbf{v}_{\mathbf{v}} \tag{11}$$

$$d_z = T_q * v_z \tag{12}$$

where B is the perpendicular spatial baseline, T is the temporal baseline, R_y is the range resolution, θ is the look angle of the SAR images, λ is the wavelength of the SAR satellite, r is the satellite altitude, d_y and d_z are the displacement of the target in horizontal and vertical directions, while ν_y and ν_z are the respected velocities. In this study, we use the following values for these variables; R_y = 60 m, θ = 35°, λ =5.6 cm, r = 700 km, ν_y =30 mm/yr, ν_z =10 mm/yr.

In the following, we use a synthetic scenario of 10 SAR images and

compare the performance of our pair selection strategy against three different approaches suggested in the literature (Fig. 3). To avoid the decorrelation error caused by pairs with very long temporal baselines, we choose a relatively short observation period that allows ignoring temporal decorrelation error. The first synthetic test (Fig. 3a) is the pairing strategy suggested by this study, the second one (Fig. 3b) considers all possible interferograms, and the third and fourth (Fig. 3c,d) is the common pairing strategies of SBAS (Berardino et al., 2002; Schmidt and Bürgmann, 2003) in the Sentinel-1 datasets (e.g. (Zhang et al., 2019)) since the spatial and temporal baseline are primarily small.

Given the mean and standard deviation of C_{ϕ} , we calculate the associated CV (Eq. (7)) for each scenario as an indicator for the overall quality of the final time series. Using the pair selection strategy in this study, we generated 25 pairs with CV of 0.15. The case, including all possible 45 pairs, yields a CV of 0.09. The corresponding values for scenarios 3 and 4 are 24 and 17 pairs and CV of 0.18 and 0.24, respectively. Although our pair section strategy results in a slightly larger CV than the case of considering full interferometric pairs, but our pair selection strategy generated 25 pairs similar to that shown in Fig. 3c, but it performs better with a smaller CV and the computation time is significantly less than the case of the full dataset, given the smaller number of interferograms.

2.2. Pixel selection

To increase the density of elite pixels, we propose a pixel selection strategy that accounts for both the permanent scatterers (PS) and distributed scatterers (DS). This algorithm identifies the high-quality DS and PS pixels. Then it performs a statistical test comparing the time series of the amplitude of DS pixels with that of adjacent PS pixels. The DS pixels that pass this test are labeled as permanent-distributed scatterers (DSp). Thus, the final set of elite pixels comprises PS and DSp pixels.

The permanent scatters (PS) are pixels with a high signal-to-noise ratio over time, which are defined by thresholding the amplitude dispersion index, $\mathcal{D}_{\mathscr{A}}$, (Ferretti et al., 2001) as:

$$\mathscr{D}_{\mathscr{A}} \equiv \frac{\sigma_{\mathscr{A}}}{\mu_{\mathscr{A}}} \tag{13}$$

where $\sigma_{\mathscr{A}}$ is the standard deviation of amplitude and $\mu_{\mathscr{A}}$ is the mean of

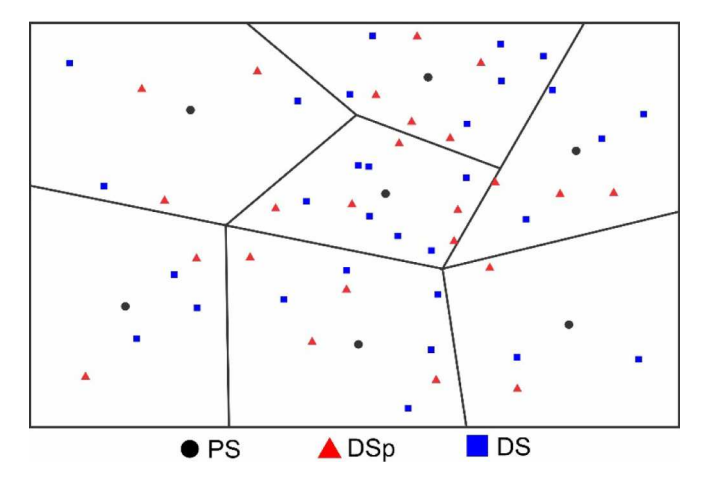


Fig. 4. Shows the procedure used for segmenting an image using Voronoi cells (black lines) based on distribution PS pixels (filled black circles). In each Voronoi cell, examples of rejected DS (filled blue square) and DSp (filled red triangle) pixels are shown. (For interpretation of the references to colour in this figure legend, the reader is referred to the web version of this article.)

the amplitude over time. We identify PS pixels as those with $\mathcal{D}_{\mathscr{A}}$ smaller than 0.3.

Similarly, to identify DS pixels, we introduce the coherence dispersion index, $\mathscr{D}_{\mathbb{Z}}$ as below:

$$\mathscr{D}_C \equiv \frac{\sigma_C}{\mu_C} \tag{14}$$

where σ_c is the standard deviation of coherence and μ_c is the mean of the coherence over time. We set this threshold at 0.4. Next, we statistically compare the time series of the amplitude of DS pixels with that of nearby permanent scatterers. To this end, we construct the Voronoi diagram based on the PS pixels distribution dividing the image into r cells associated with PS pixels. Next, identify the DS pixels within each Voronoi cell. The size of the Voronoi cell is a function of the density of PS pixels; in areas with sparse PS distribution, their size may increase. Given an arbitrary PS pixel with a temporal amplitude standard deviation of σ_{PS} and a set of q DS pixels with temporal amplitude standard deviations

 $\{\sigma_{DS}^1, \sigma_{DS}^2, \dots, \sigma_{DS}^q\}$ within the associated Voronoi cell, we perform a test for homoscedasticity (Goldfeld and Quandt, 1965), which examines if the temporal amplitude variance (i.e., square of standard deviation) of DS pixels within a Voronoi cell is statistically comparable to that of its PS pixel. Considering the ratio of the PS and DS variances,

$$F = \left(\sigma_{DS}^{i}/\sigma_{PS}\right)^{2} i = 1, \dots q$$
(15)

F approximates a Fisher probability distribution function with (n-1; n-1) degree of freedom (Meyer, 1970). The null hypothesis states that PS and DS variances are equivalent within a Voronoi cell, and we test this hypothesis at a 0.01 significance level. If the value of statistics shown in Eq. (15) is larger than its theoretical value obtained from the Fisher distribution, the null hypothesis is rejected. Otherwise, the test passes, and the DS becomes a DSp. This procedure is illustrated schematically in Fig. 4 and Fig. 5. The time series of the amplitude of a DSp pixel has a narrow probability density function (PDF) similar to that of a PS but with a smaller mean (Fig. 5). In contrast, the rejected DS has a wide distribution with a smaller mean.

2.3. Atmospheric delay correction

Atmospheric delay is composed of hydrostatic delay, wet delay, liquid, and ionospheric delay. Here, we focus on hydrostatic and wet delays, given that the contribution from the liquid term is often minor, and the influence of ionospheric delay in the C-band is sometimes negligible due to the inverse proportionality of dispersive phase and frequency of the electron (Goldfeld and Quandt, 1965). However, the ionospheric artifacts can be significant sometimes, but these can be mitigated using methods such as split-band spectrum algorithms (Gomba et al., 2017). Part of the hydrostatic and wet delay is correlated with topography. The remainder is often characterized as a stochastic delay (Hanssen, 2001), which correlates to a given spatial length, and its behavior in a SAR interferogram can be readily described using fractal statistics (Hanssen, 2001).

To devise the delay correction approach, our rationale is that the atmospheric delay is independent of the temporal baseline in contrast to the surface deformation. Thus, considering m pairs created, we identify a set of n-1 pairs with minimum decorrelation error, including

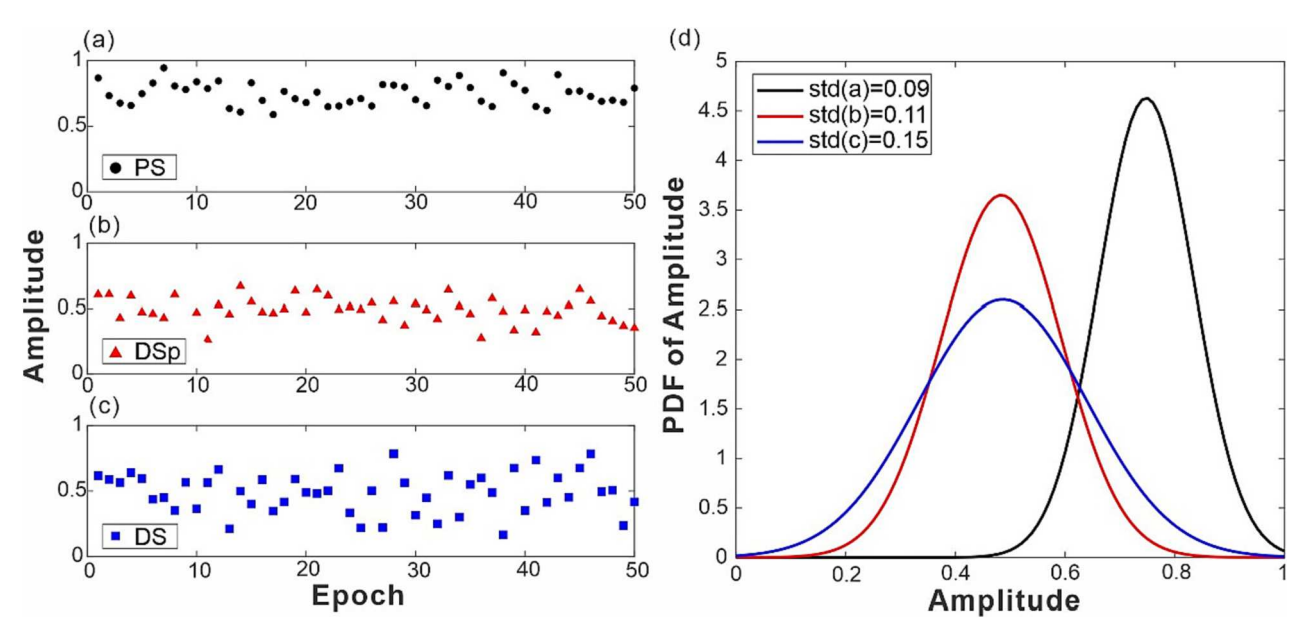


Fig. 5. Normalized time series of interferometric phase amplitude for a permanent scatterer (PS) pixel with a standard deviation of 0.09, (b) a permanent-distributed scatterer (DSp) pixel with a standard deviation of 0.15, (d) the associated probability density distributions.

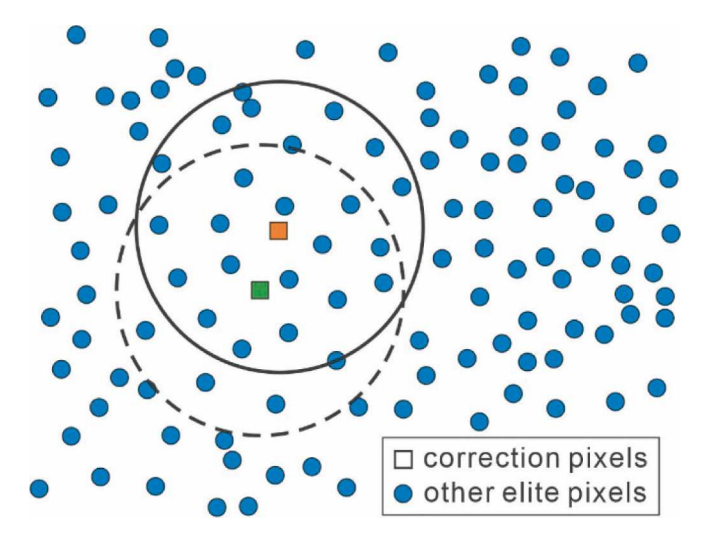


Fig. 6. Sketch showing implemented algorithm for atmospheric delay correction using patch-wise 2D smoothing spline. Blue circles and rectangles are the elite pixels. Rectangles are two adjacent pixels used to demonstrate how the atmospheric delay works. Circles in black dashed and solid lines centered at the location of squared elite pixels, whose radius indicates the correlation length of the atmospheric delay. Pixels within a black circle are used to fit the ramp and estimate the atmospheric delay for the center pixel. (For interpretation of the references to colour in this figure legend, the reader is referred to the web version of this article.)

interferograms of short temporal and perpendicular baselines. To this end, we apply a minimum spanning tree (MST) algorithm (Feng et al., 2017), which minimizes the following cost function:

$$C_{MST} = \rho_s \cdot \rho_t \tag{16}$$

The advantage of exploring MST pairs for this correction is that they include a minimal deformation signal and residual DEM errors, while they are affected by the same atmospheric delay as the original interferometric dataset. Next, we draw on the work by (Duchon, 1977), demonstrating that smooth spline functions could effectively approximate fractal-like signals and employ a patch-wise 2D smoothing spline to approximate the atmospheric delay in each MST interferogram (Fig. 6). In this approach, an optimum spline function $f(X_i, Y_i)$ is found that minimizes the following cost function (Gu, 2002):

$$C_{spline} = \left\| \delta \phi - f \right\|^2 + \lambda f' \tag{17}$$

where $\delta \phi$ is the unwrapped phase, f is a 2D spline function that is differentiable, and $\lambda > 0$ is the smoothing parameter. An infinite set of functions f exists that minimizes Eq. (17) depending on the choice of λ . Thus function f is obtained numerically following some assumptions. Here, we broadly follow the approach of (de Boor, 1978), in which we find a numerical form of function f that maintains a certain level of smoothness and closeness to data points. To this end, we make the following assumptions, (i) within a small area (e.g., $5 \text{ km} \times 5 \text{ km}$), the atmospheric delay can be approximated by a ramp (Ferretti et al., 2001), and (ii) within interferograms of short temporal baseline, the surface deformation to atmospheric delay ratio is low, while the atmospheric delay is independent of temporal baseline. As shown in Fig. 6, we consider a sliding window of 5 km \times 5 km centered at the pixel location (X_i, Y_i) , and fit a plane to the unwrapped phase value of pixels within the window. Evaluating this plane at the pixel location (X_i, Y_i) yields the value $f(X_i, Y_i)$. Next, we slide the window to the adjacent pixel and repeat the operation above, which eventually yields the evaluations of function f for every pixel in the interferogram. It is straightforward to show that the significant overlap between adjacent sliding windows satisfies both

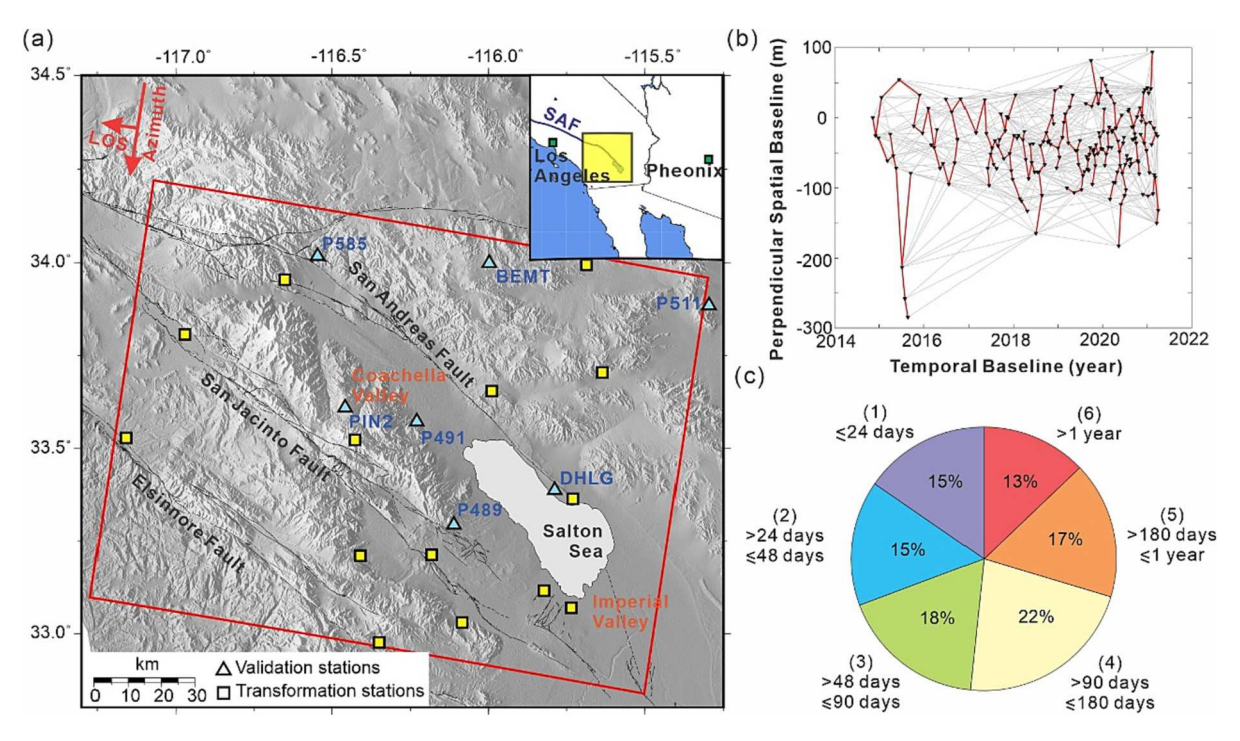


Fig. 7. Study area and interferometric baseline plots. (a) Study area. The inset map shows the southwest United States, with our study area marked by the yellow box. The red box indicates the SAR scene. The shaded relief topographic map is from SRTM 90 m DEM and the overlaid faults are from the USGS quaternary fault map. The rectangles are the GNSS stations used for affine transformation and the triangles are the GNSS stations used for validation. (b) Interferometric baselines plot. The filled triangles are the SAR acquisitions, and the gray lines are the interferometric dataset used for generating time series. The red lines are pairs identified using a minimum spanning tree algorithm used for atmospheric delay correction and elite pixel selection. (c) The pie chart shows the distribution of the temporal baselines of the interferograms used in this study. (For interpretation of the references to colour in this figure legend, the reader is referred to the web version of this article.)

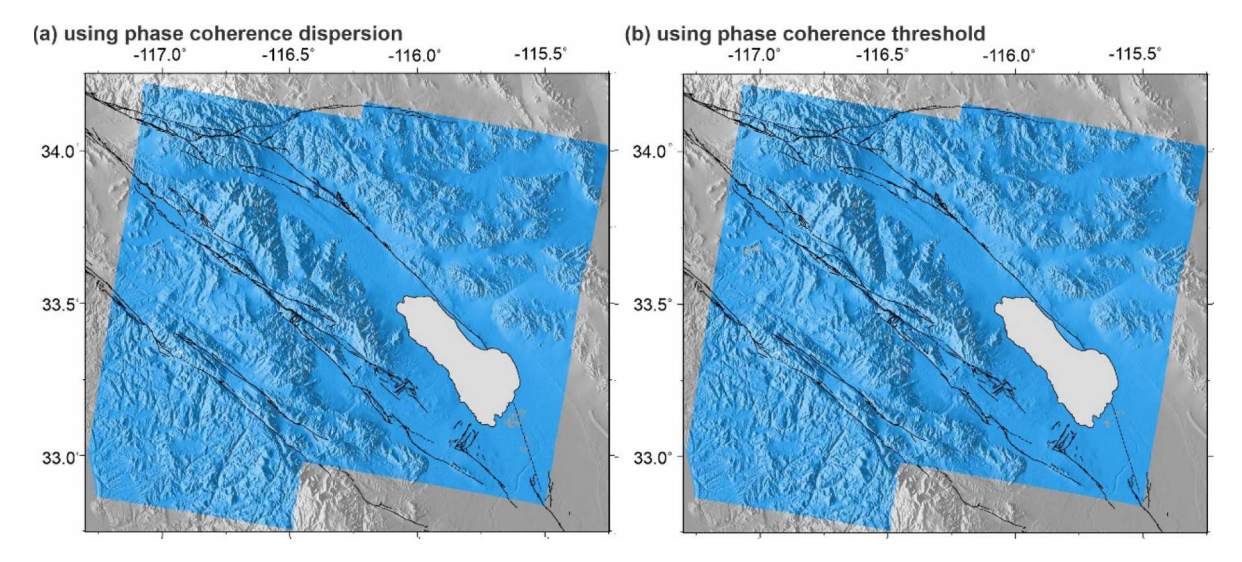


Fig. 8. DS pixels selection using (a) phase coherence dispersion (this study) (b) phase coherence threshold (conventional methods).

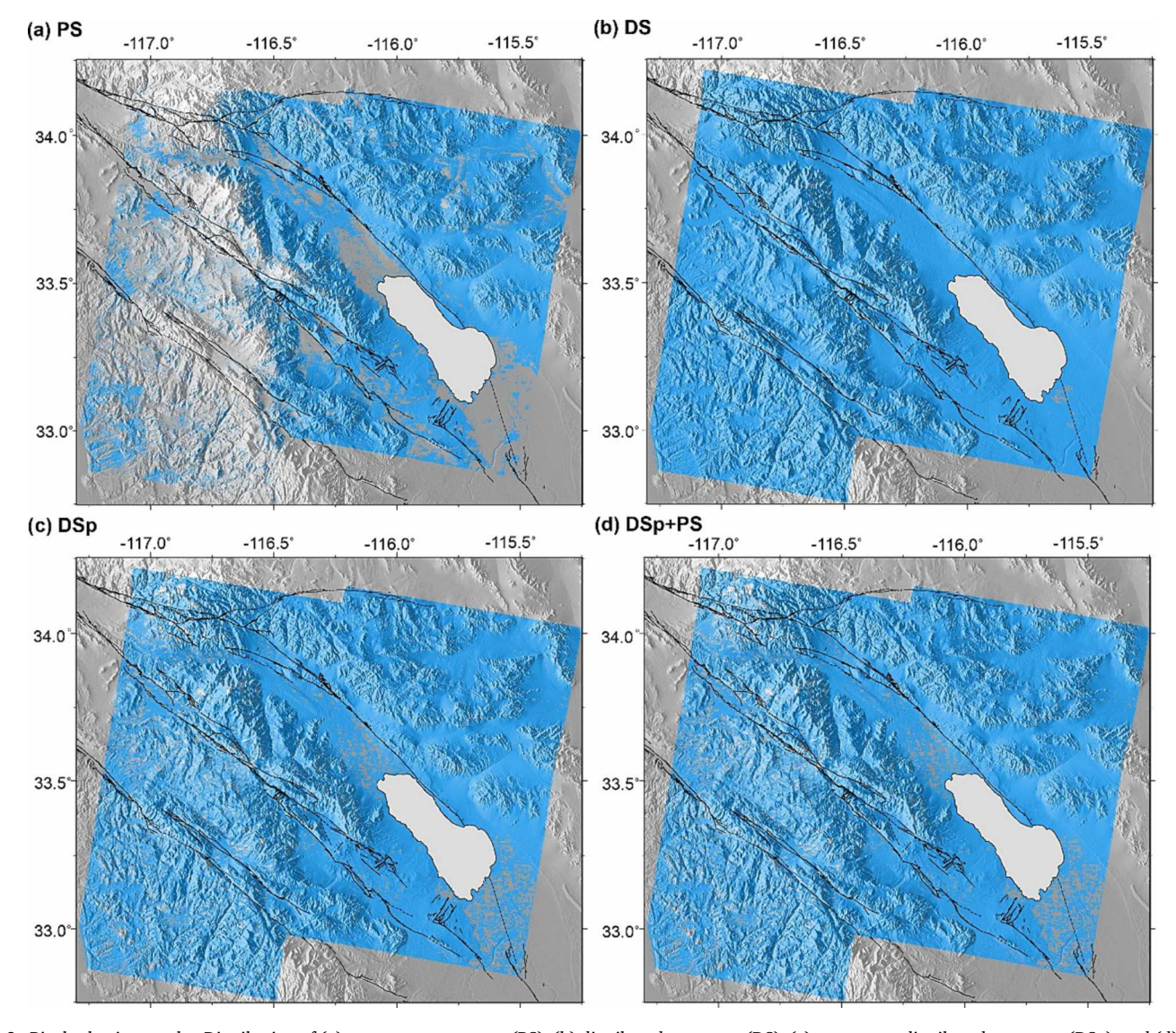


Fig. 9. Pixel selection results. Distribution of (a) permanent scatterers (PS), (b) distributed scatterers (DS), (c) permanent-distributed scatterers (DSp), and (d) elite pixels obtained by merging DSp and PS sets.

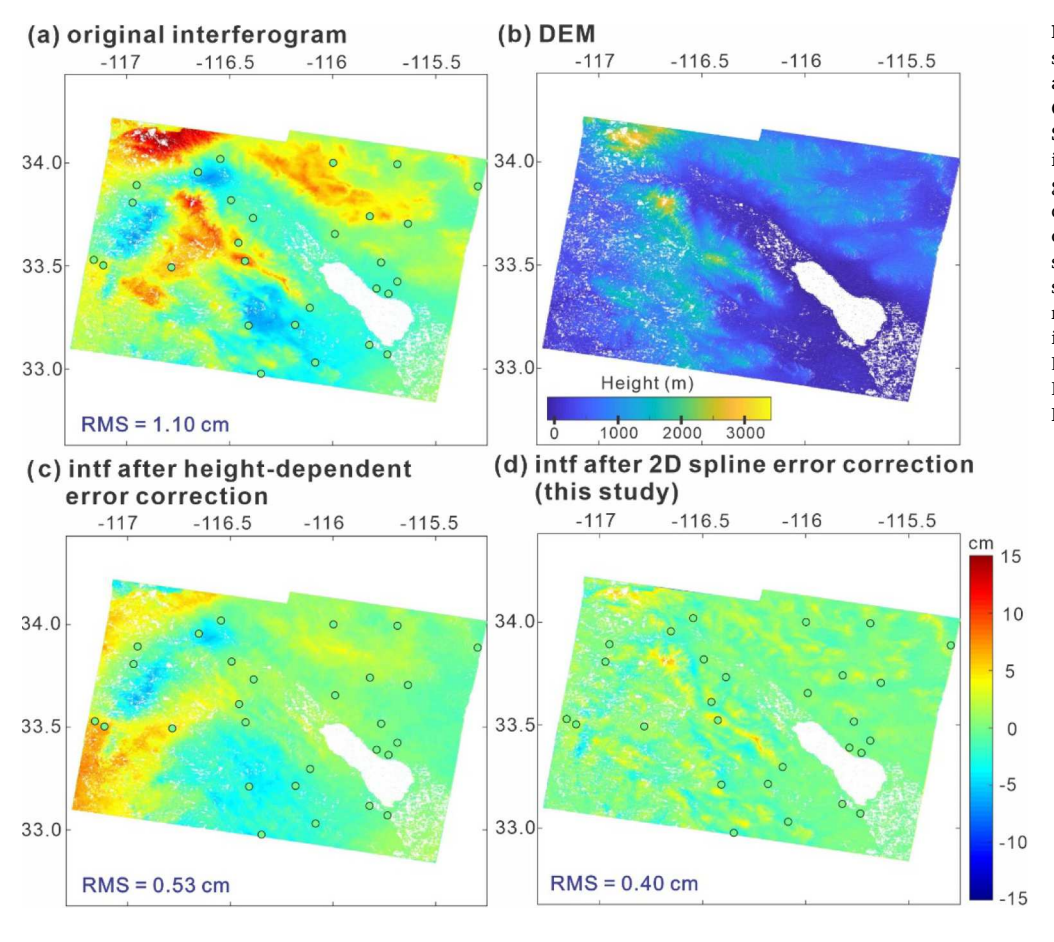


Fig. 10. Example of unwrapped phase spanning 2014/11/10-2014/12/28 and applied atmospheric delay corrections. (a) Original unwrapped interferogram, (b) SRTM 90 m DEM oversampled on the interferogram. (c) Unwrapped interferogram after correction using a heightdependent filter. (d) Unwrapped interferogram after correction using our 2D smoothing spline filter. Circles show GNSS stations colour-coded to their displacement for the interval covered by the interferogram shown in panel a. RMS: Root Mean Square of difference between InSAR and GNSS observation projected on LOS direction.

smoothness of function f and closeness to data points, as required by Eq. (17) (Graham and Hell, 1985). After estimating the spline functions $\{f_1(X_i,Y_i),...,f_{n-1}(X_i,Y_i)\}$, we obtain the corrected unwrapped phase $\{\widehat{\delta\phi}_1,...,\widehat{\delta\phi}_{n-1}\}$ for MST pairs by subtracting its corresponding spline f from the unwrapped phase $\delta\phi$. To low-pass filter the corrected unwrapped phase of a pixel at a location (X_i,Y_i) , following (Berardino et al., 2002), we fit a temporal quadratic polynomial function to its corrected phase measurements $\{\widehat{\delta\phi}_1(X_i,Y_i),...,\widehat{\delta\phi}_{n-1}(X_i,Y_i)\}$ and then evaluate this quadratic function at the time of n SAR acquisitions to obtain the time series of corrected phase change, $\widehat{\phi}^T$ with respect to the time of the first acquisition:

$$\widehat{\boldsymbol{\phi}}^T = [0, \widehat{\boldsymbol{\phi}}_1, ..., \widehat{\boldsymbol{\phi}}_{n-1}] \tag{18}$$

Additionally, applying Eq. (3) to the original interferometric phase observations, $\{\delta\phi_1,...,\delta\phi_{n-1}\}$, yields a time series of uncorrected ϕ^T

$$\boldsymbol{\phi}^{T} = [0, \phi_{1}, \dots, \phi_{n-1}] \tag{19}$$

The difference of Eqs. (18) and (19) yields the atmospheric delay correction time series as follows

$$\mathbf{E}^{T} = \boldsymbol{\phi}^{T} - \widehat{\boldsymbol{\phi}}^{T} = \mathbf{E}_{atm}^{T} + \mathbf{E}_{noise}^{T} \tag{20}$$

We further detrend E^T and apply a 2D Gaussian filter of radius 5 km to reduce the effect of E^T_{noise} and obtain E^T_{atm} , following (Ferretti et al., 2001). The time series of E^T_{atm} obtained from n-1 MST pairs is used to correct the entire interferometric dataset, comprising m interferograms.

The algorithm above may fail to correct a portion of the topography-correlated delay with a short spatial wavelength. Thus, we further apply the method of (Shirzaei and Bürgmann, 2012), which uses wavelet transforms to identify and remove the residual topography-correlated atmospheric delay. To this end, we use Coiflet wavelets of order 5 at 1

level of decomposition, which results in wavelet function with support twice the ground dimension of a multilooked SAR pixel (Shirzaei and Bürgmann, 2012).

Note that given n images, only n-1 independent pairs can be generated, which are the minimum requirements for performing the analysis above. In addition to n-1 MST pairs, one can include other interferograms to increase the degree of freedom, but additional pairs are an algebraic combination of the MST interferograms. Thus, they do not carry new information on the atmospheric delay content, while their noise contents vary due to SAR geometry, surface characteristics, and baselines. We found that the n-1 MST pairs are sufficient to estimate atmospheric delay, though the estimate is not robust to outliers and noise due to a lack of redundancy. However, since the original interferometric dataset, corrected using MST pairs, has significant redundancy, any remaining outliers will be adjusted when the final time series is generated.

3. Experimental results

We apply the proposed framework to 3 SAR datasets acquired over two different terrains with spatially and temporally variable deformation patterns. The first study case is in southern California (Fig. 7a) and is characterized by a considerable surface elevation change and different textures, such as bare land and agriculture. Several active faults also run through this area, including the San Andreas Fault and the San Jacinto Fault. We apply the presented processing algorithm shown in Fig. 1 and use 195 Sentinel-1 SAR datasets acquired from November 2014 to April 2021 in descending orbit, covering the study area highlighted by a red box in Fig. 7a. To reduce the dataset size, we apply multilook factor of 30 in range and 6 in azimuth, resulting in a pixel size of ~69.9 by 83.9 m. Using the method described in section 2.1, 1113 interferograms are

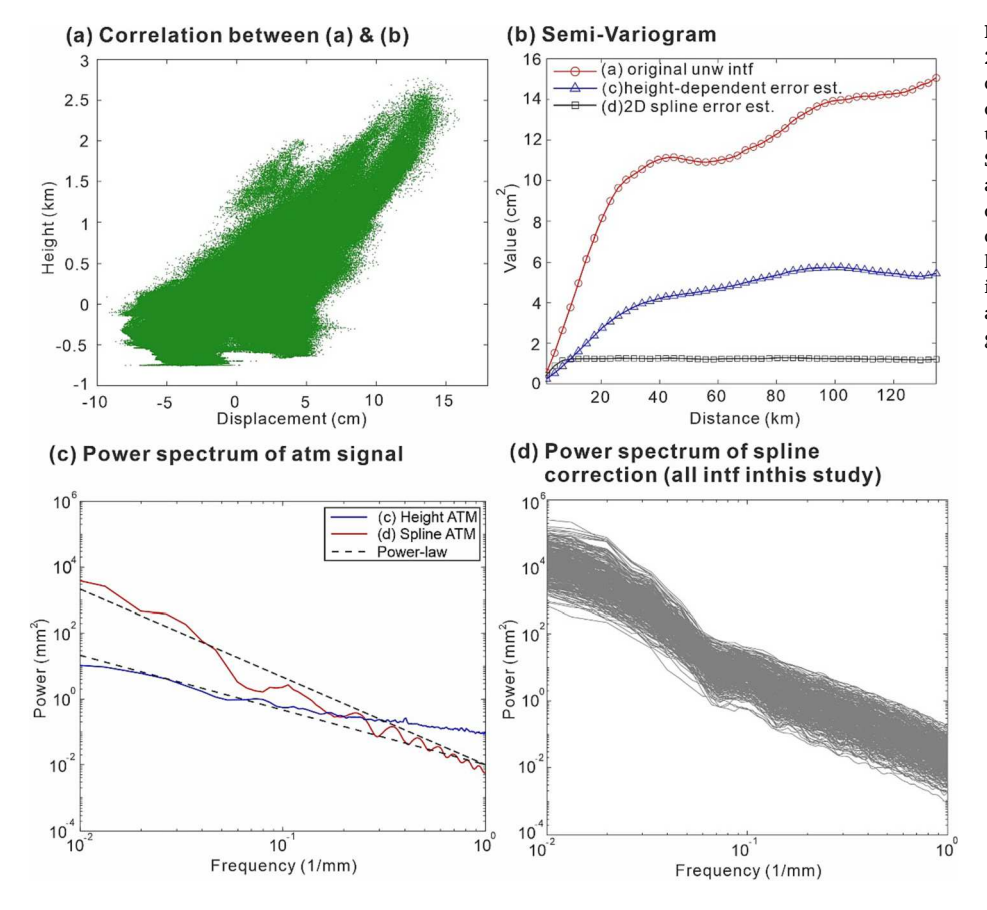


Fig. 11. Example of unwrapped phase spanning 2014/11/10–2014/12/28 and applied atmospheric delay corrections. (a) Bivariate plot showing the correlation between original interferogram unwrapped phase and the SRTM 90 m DEM, (b) Semivariogram generated for the panels Fig. 10 a, c and d, (c) Power spectrum of the atmospheric delay corrected using 2D smoothing spline and height dependent filters in Fig. 10 panels c and d. Black lines indicate –5/3 and – 8/3 power-law behaviors (Hanssen, 2001), (d) Power spectrum of the atmospheric delay corrected for all the interferograms using 2D smoothing spline filter.

generated with temporal baseline and spatial baselines <3 years and 150 m, respectively, consisting of different temporal baseline pairs (Fig. 7c) to prevent the potential systematic bias (Ansari et al., 2020) while avoiding pairs with too long temporal baselines affected by decorrelation noise. We also visually inspect to ensure long baseline pairs are of good quality. The baseline plot of the entire interferometric dataset is shown by gray lines in Fig. 7b, where MST pairs are highlighted in red. Elite pixels selection follows the procedures in section 2.2. Firstly, we identify DS pixels using the coherence dispersion index (Eq. (14)) and compare the results with that based on average temporal coherence. Fig. 8 shows the spatial distribution of the DS pixels from the two approaches, which are visually indistinguishable with a similar number of elite pixels. We conclude that either approach is suitable for identifying the DS pixels in our study area. We, next, identify PS pixels. The PS and DS datasets include 1,279,028 and 2,370,969 pixels (Fig. 9). As seen in Fig. 8, in the northern areas of the Salton Sea, including farms, the PS pixels are distributed sparsely, while DS pixels are abundant. The refined distribution of DS pixels, namely the DSp pixels, includes 1,920,533 pixels, and many of the high-quality DS pixels in the north of the Salton Sea are preserved. The final population of elite pixels is obtained by combining DSp and PS pixels comprising 1,920,545 pixels. The atmospheric delay time series is estimated using MST pairs, and accordingly, the entire interferometric dataset is corrected. We visually inspect MST pairs to ensure they are of good quality. Fig. 10 shows an example of a corrected unwrapped interferogram spanning 2014/11/ 10–2014/12/28. The unwrapped interferogram (Fig. 10a) includes phase values with a significant spatial variation that partly correlates with the DEM (Fig. 10b, c). For comparison, we first correct the unwrapped phase using a conventional approach that removes the height-dependent component of the unwrapped phase (Duchon, 1977) (Fig. 10d). Next, we apply our approach based on spatial patch-wise 2D smoothing spline (Fig. 11a). To evaluate the accuracy of different

correction approaches, we use independent observation of Global Navigation Satellite System (GNSS) displacement within the same time frame, projected on the line-of-sight (LOS) direction. The standard deviation of the difference between GNSS displacement and the original unwrapped interferogram, height-dependent corrected interferogram, and 2D smoothing spline corrected interferogram are 1.10 cm, 0.53 cm, and 0.40 cm, respectively. Our approach reduces the majority of longwavelength and topography-correlated phase components (Fig. 11b), and the corrected phase agrees well with independent measurements. To further assess the spatial patterns of atmospheric delay, we employ a spatial structure-function (Hanssen, 2001) in the form of a semivariogram. Fig. 11b shows the semivariogram of the original unwrapped interferogram and the height-dependent and 2D smoothing splinecorrected ones. The original interferogram is characterized by signals correlated at distances >100 km. The corresponding correlation lengths for height-dependent and 2D smoothing spline corrected ones are 30 km and 5 km, respectively.

Furthermore, the spectral properties of the corrected atmospheric delay are investigated. Fig. 11c compares the power spectrum of the subtracted atmospheric delay using height-dependent and 2D smoothing spline correction approaches. The study by (Hanssen, 2001) demonstrates that atmospheric turbulence can be described by power-law behavior with slopes varying between -5/3 and -8/3, which, for reference, are shown in Fig. 11c. As seen, the atmospheric correction using the 2D smoothing spline approach agrees well with the theoretical power-law behavior proposed for atmospheric turbulence. Fig. 11d shows the power spectrums of the corrected atmospheric delay for the entire atmospheric dataset, all of which show a slope within the range of -5/3 and -8/3. Following atmospheric delay correction, we identify and remove the long-wavelength signal in the spatial domain, possibly due to ionospheric delay or residual orbital error following (Shirzaei and Walter, 2011). The corrected unwrapped interferograms are inverted

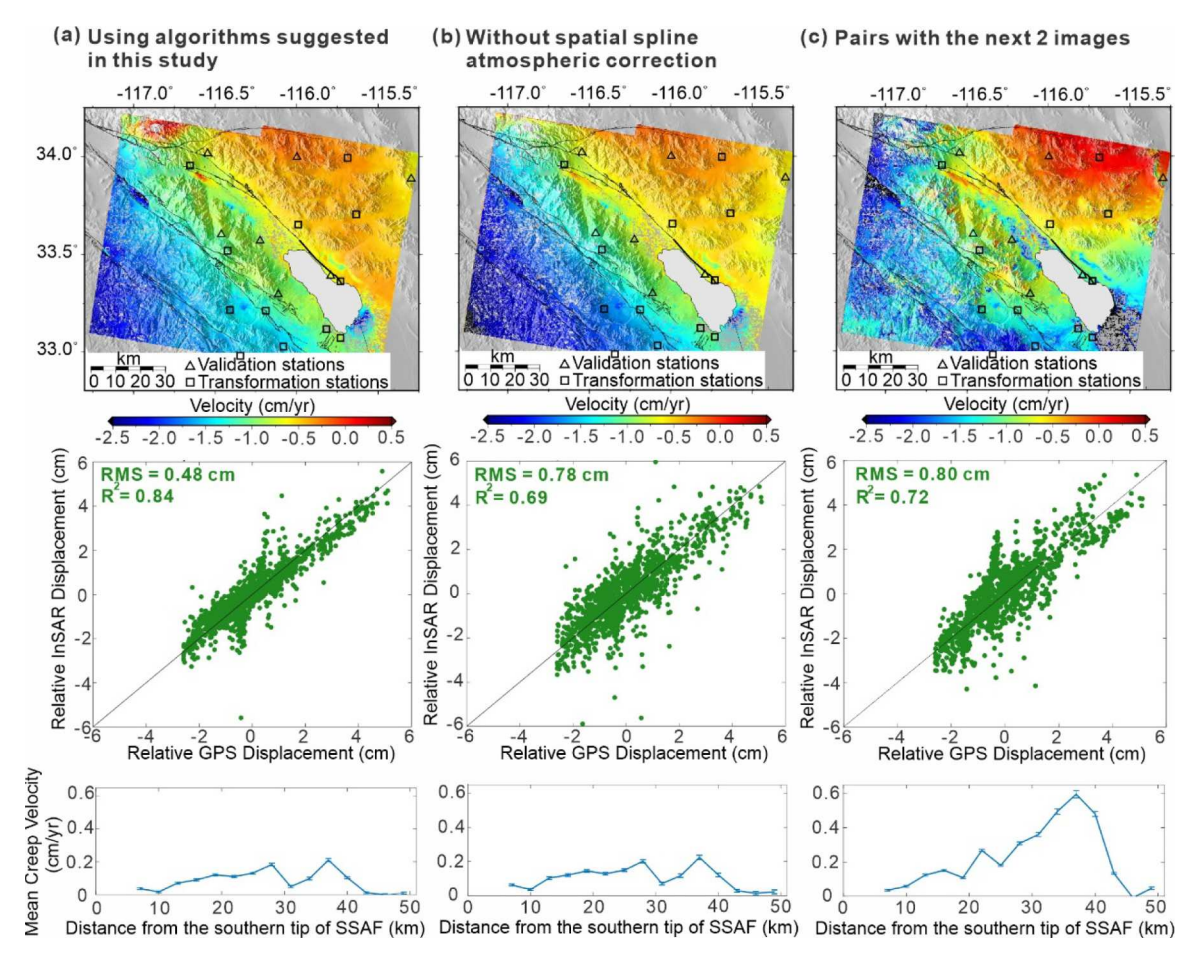


Fig. 12. InSAR LOS velocity for period late 2014 to early 2021 and validations of the descending frame of the southern San Andreas Fault. (a) LOS velocity following the algorithm presented in this study. Bi-variable plot showing the association between the InSAR time series and GNSS validation stations (triangles in Fig. 7), also root mean square of differences and coefficients of variations are provided. Lowest panel shows the LOS creep rate and standard deviation along the creeping segment of San Andreas Fault. A thick black line shows the creeping segment in the top panel. (b) Same as panel a, without applying 2D smoothing spline filter for atmospheric error correction. (e) Same as panel a, but considering interferometric dataset created using the following two images and applying 2D smoothing spline filter for atmospheric error correction.

using Eq. (3) to obtain the time series of surface displacement for each elite pixel. The weight matrix is proportional to the time series of interferometric coherence associated with each elite pixel. We used observations from the GNSS network to restore the long-wavelength deformation signals that were possibly removed while correcting for ionospheric and residual orbital errors. We obtain these datasets from the Nevada Geodetic Laboratory of the UNAVCO PBO network (Blewitt et al., 2018), including 21 stations within our study area, and apply the Greedy Automatic Signal Decomposition algorithm (Bedford and Bevis, 2018) to avoid the noise from daily solutions. We randomly select 14 stations to determine the parameters of an affine transformation, including two rotations, one translation, and one scale suitable for transforming the LOS displacement field and restoring the longwavelength signals. The remaining 7 GNSS stations are independent observations that validate our proposed multitemporal SAR interferometric analysis. We note that the horizontal observations at 7 GNSS stations are not entirely independent from the 14 stations used for restoring long wavelengths. However, the vertical component often varies locally and can differ significantly from nearby stations.

The estimated LOS velocities for cases with and without applying our atmospheric corrections are also shown in Figs. 12a and b. Overall, the two results are comparable; for instance, the Coachella Valley is affected by a similar maximum LOS rate. However, our approach successfully maintains localized signals, such as creep along the San Andreas Fault, as shown in the lowest panel of Fig. 12a. Compared with the previous

study that used the SBAS approach in the southern San Andreas Fault (Fialko, 2006; Lindsey and Fialko, 2013; Tymofyeyeva et al., 2019; Xu et al., 2018), our result can successfully extract the displacement and velocity of elite pixels within the Coachella Valley while the other study shows noisy data points or lack of pixels within the valley due to low coherence.

We compare the LOS displacement time series against the independent GNSS datasets following projecting 3D displacements onto the radar LOS (Figs. 12a and 13). To this end, we identified elite pixels within 500 m of each GNSS station and averaged their values to obtain a corresponding LOS value. We find a root mean square of 0.48 cm for the difference between our LOS displacement time series and that obtained from GNSS with a 0.84 coefficient of determination (Fig. 12a). The corresponding values for the case without atmospheric correction are 0.78 cm and 0.69, respectively (Fig. 12b). We have performed an additional test using the interferometric dataset created using the following two images (Zhang et al., 2019), in which we also apply our atmospheric correction approach. Results are shown in Fig. 12c. The LOS velocity map appears noisy, and the validation against GNSS measurements yields a root mean square error of 0.80 cm for the time series differences. Fig. 13 also shows the comparison between the InSAR time series and that of GNSS. At most stations, our approach performs well, which a root mean square error of difference smaller than 0.5 cm. These tests indicate the success of our approach in reducing atmospheric errors and retrieving surface deformation at high accuracy and

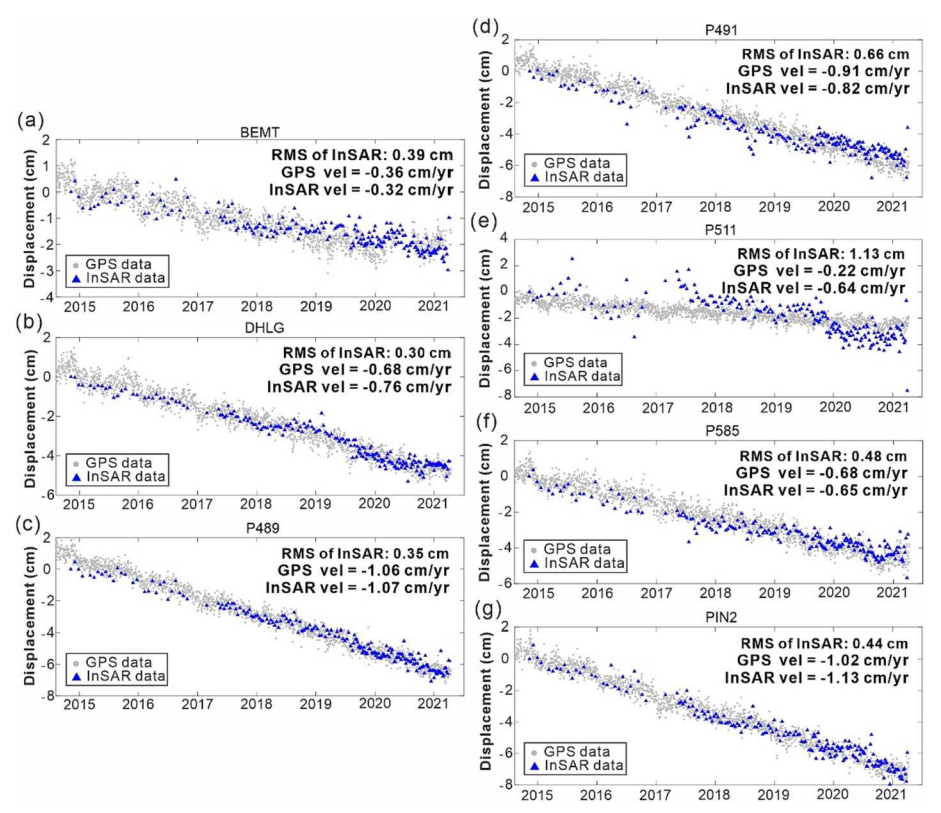


Fig. 13. Validating InSAR time series versus that of GNSS stations with the root-mean-square of InSAR data and the velocity estimate of GNSS and InSAR data. Gray dots are the GNSS daily solutions, and blue triangles correspond InSAR time series. We used the average value of pixels within a 500 m radius of each GNSS station for this comparison. To further reduce temporal noise in InSAR time series, one can apply a triangular, rectangular, or Gaussian filter following (Berardino et al., 2002; Ferretti et al., 2001), which we did not apply in this case study. (For interpretation of the references to colour in this figure legend, the reader is referred to the web version of this article.)

precision.

As for the second test, we apply an identical processing pipeline and parameters to the ascending pass of Sentinel-1 over the same site used in our first test, namely southern California. We used 149 SAR images and generated 845 interferograms from mid-2015 to mid-2021. The final LOS velocity is shown in Fig. 14 (a) and the time series is validated against independent GNSS observations, shown in Fig. 14(a). Despite the relative northwest-southeast orientation of the fault systems, which is unfavorable concerning the ascending satellite flight direction, the obtained velocity field is consistent with that of the descending track shown in Fig. 12(a) with a standard deviation of 0.48 cm for the difference between InSAR LOS time series and independent GNSS observations.

As for the third test, we chose the city of Los Angeles and analyzed 247 SAR images acquired in descending orbit of Sentinel-1 satellites from early 2016 to mid-2022. For this case study, we applied a multilooking factor of 12 and 2 in range and azimuth directions, corresponding with a pixel size of \sim 25 m by \sim 25 m on the ground. Assuming a maximum temporal baseline of 300 m, we created 1054 pairs using this dataset, comprising 3,039,151 elite pixels. The final LOS velocity and validation against independent GNSS observation are shown in Fig. 14 (b). We found a standard deviation of 0.30 cm for the difference between the InSAR and GNSS time series. In order to further investigate the vertical land motion across Los Angeles, we created a horizontal velocity field from observation of GNSS stations within the study area, oversampled it on the location of elite pixels, and then projected it onto the LOS direction. We then removed them from LOS velocities and time series. Next, we projected back the residuals in the vertical direction. Fig. 15 shows the vertical land motion rate and sample time series, comprising various uplifting and subsiding features consistent with earlier studies (Brooks et al., 2007; Lanari et al., 2004; Riel et al., 2018; Shen and Liu, 2020). We observe a subsidence rate of 0.79 cm/yr over the Santa Ana area (site A) and about 0.23 cm/yr uplift nearby (site B). The time series of both sites, A and B, show seasonal variations likely due to groundwater level fluctuations within the aquifers (Riel et al., 2018).

Site C shows a rate of -0.34 cm/yr at Seal Beach and site D, with a rate of 0.42 cm/yr at Long Beach, near the Newport-Inglewood Fault. Sites E and J, with rates of 1.04 cm/yr and -0.51 cm/yr, are located at the Wilmington oil field. A strong uplift signal of rate 1.04 cm/yr was observed at site E, likely associated with enhanced oil recovery. Site J shows a subsidence signal of -0.51 cm/yr. Site F is located at the center of the Los Angeles area, showing slight subsidence of -0.30 cm/yr. Sites G and H are located near the Hollywood Fault. Site H shows a strong uplift signal of 0.57 cm/yr, while site G subsidies at a rate of -0.5 cm/yr. Site I is located in Ontario and subsides at a rate of -0.6 cm/yr.

4. Discussion and conclusions

The primary issues with employing an SBAS-type processing algorithm include a somewhat arbitrary pair selection strategy, a non-uniform DS pixels quality, and a lack of an effective atmospheric error correction approach. To overcome some of these limitations, we presented an improved multitemporal InSAR algorithm to perform an advanced analysis of high-resolution datasets such as those provided by Sentinel-1A/B.

Our pair selection strategy leverages the Delaunay Triangulation method and combines it with dyadic downsampling to create a random but limited set of triplets, including interferograms with a wide range of temporal baselines. Using parametric analysis of variance-covariance matrices and numerical case studies, we demonstrated that our approach efficiently retrieves surface deformation signals at high accuracy and precision.

Our elite pixel selection approach adds to the growing literature on the combined analysis of DS and PS pixels (Ferretti et al., 2011; Hooper, 2008). The novel aspect of our approach is performing hypothesis testing based on Fisher distribution to examine the similarity between the temporal distribution of the interferometric amplitude of DS and PS pixels. Unlike pixel selection algorithms that rely only on interferometric coherence, our approach applies to full resolution and multilooked interferogram analysis since it exploits interferometric

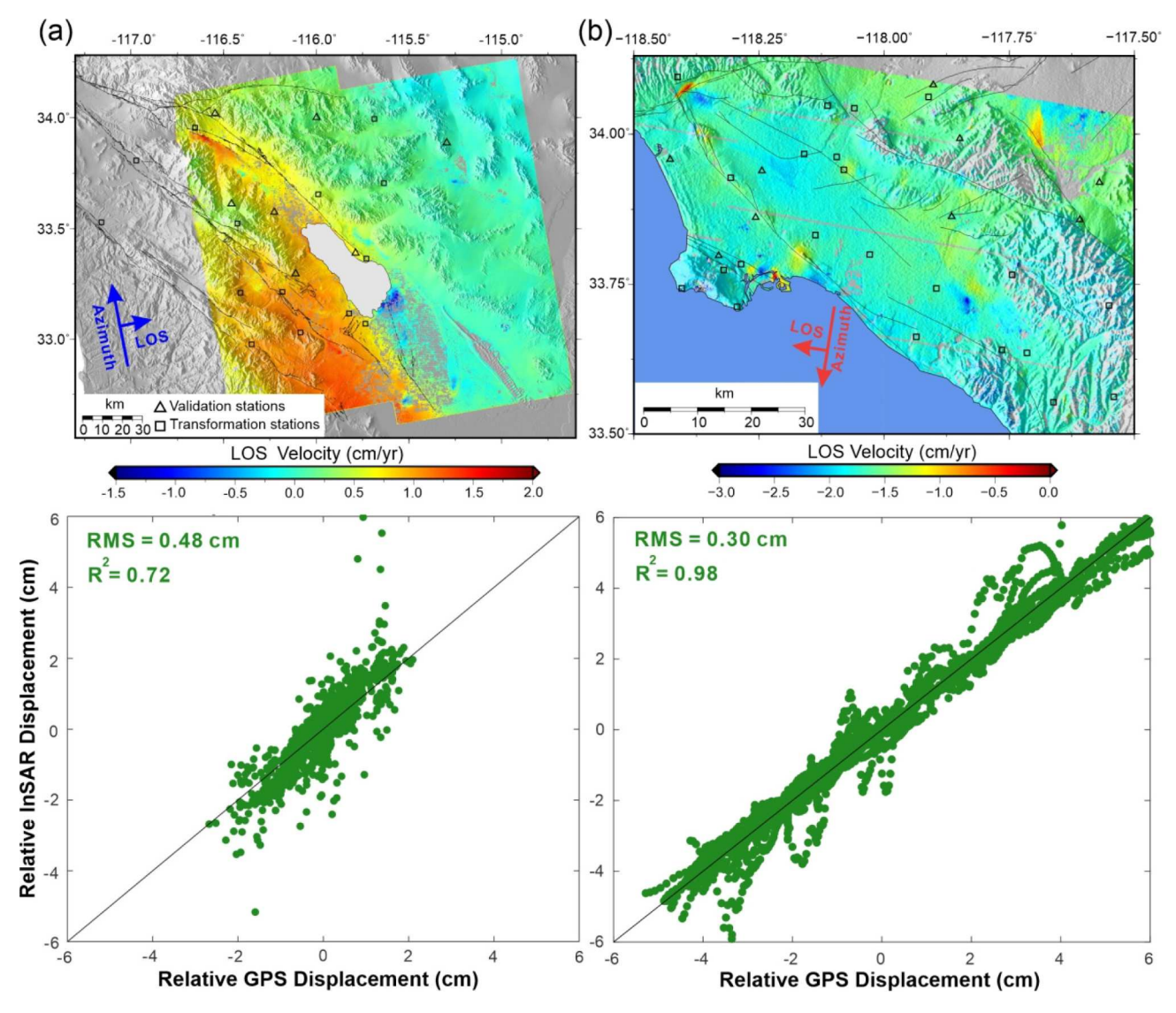


Fig. 14. Experimental results for test cases two and three. (a) Ascending track of southern California, (b) Descending track of Los Angeles. LOS velocity and bivariable plots showing the association between the InSAR time series and GNSS validation stations (triangles in top panels), root-mean-square of differences, and coefficients of variations are provided. The blank lines marking the burst limits in Los Angles case study are rows of null entries added after discarding the recording of one of the overlapped bursts to avoid artefect due to geometric and radiometric differences at the burst overlaps. This null line is not visible in the other case studies due to larger multilooking factor, resulting in lower resolution.

amplitude and coherence information. This is because the interferometric coherence is independent of the number of looks (Lee et al., 1994). However, the issue of the applicability of the SBAS method to the analysis of interferograms at full resolution is addressed by (Lanari et al., 2004).

Our atmospheric delay correction approach explores the natural behavior of atmospheric turbulence in a SAR interferogram and effectively removes the hydrostatic and wet components of the delay, which are characterized by fractal statistics. Our approach requires that the deformation signal correlates with the temporal baseline and/or its spatial pattern differs from that of fractals. This requirement does not restrict the applicability of our approach, as it may be violated seldom only by rapid deformation caused, for instance, by an earthquake. In practice, the interferograms spanning an earthquake often are not corrected for the atmospheric delay due to the large amplitude of the signal. Nevertheless, we recommend examining the power spectrum of the corrected atmospheric delay to ensure it follows the theoretical power-law statistics suggested for atmospheric turbulence.

Here, we used the WabInSAR framework to implement our new

algorithms. However, they can be readily implemented in any SBAS-type processing workflow. We note that not accounting for all possible interferometric pairs might still cause phase inconsistencies (de Zan et al., 2015). Other approaches to overcome this issue include incorporating all possible interferograms to estimate the systematic bias by investigating their statistical characteristics using the phase triangulation algorithm (Ferretti et al., 2011; Guarnieri and Tebaldini, 2008), eigenvalue decomposition (EVD) (N. Cao et al., 2016; Fornaro et al., 2015), eigendecomposition-based maximum likelihood-estimator of interferometric phase (EMI) (Ansari et al., 2018).

We conclude that (i) implementing a careful pair selection strategy such as Dyadic Delaunay Triangulation can significantly reduce computation load and result in a deformation field with precision comparable to that obtained from analyzing all possible pairs, excluding those affected by temporal decorrelation. (ii) Statistical comparison of the permanent and distributed scatterers is a practical approach for maximizing the population of elite pixels. (iii) Atmospheric delay in SAR interferometry can be effectively estimated and removed using a filter based on 2D smoothing splines. (iv) Compared with GNSS

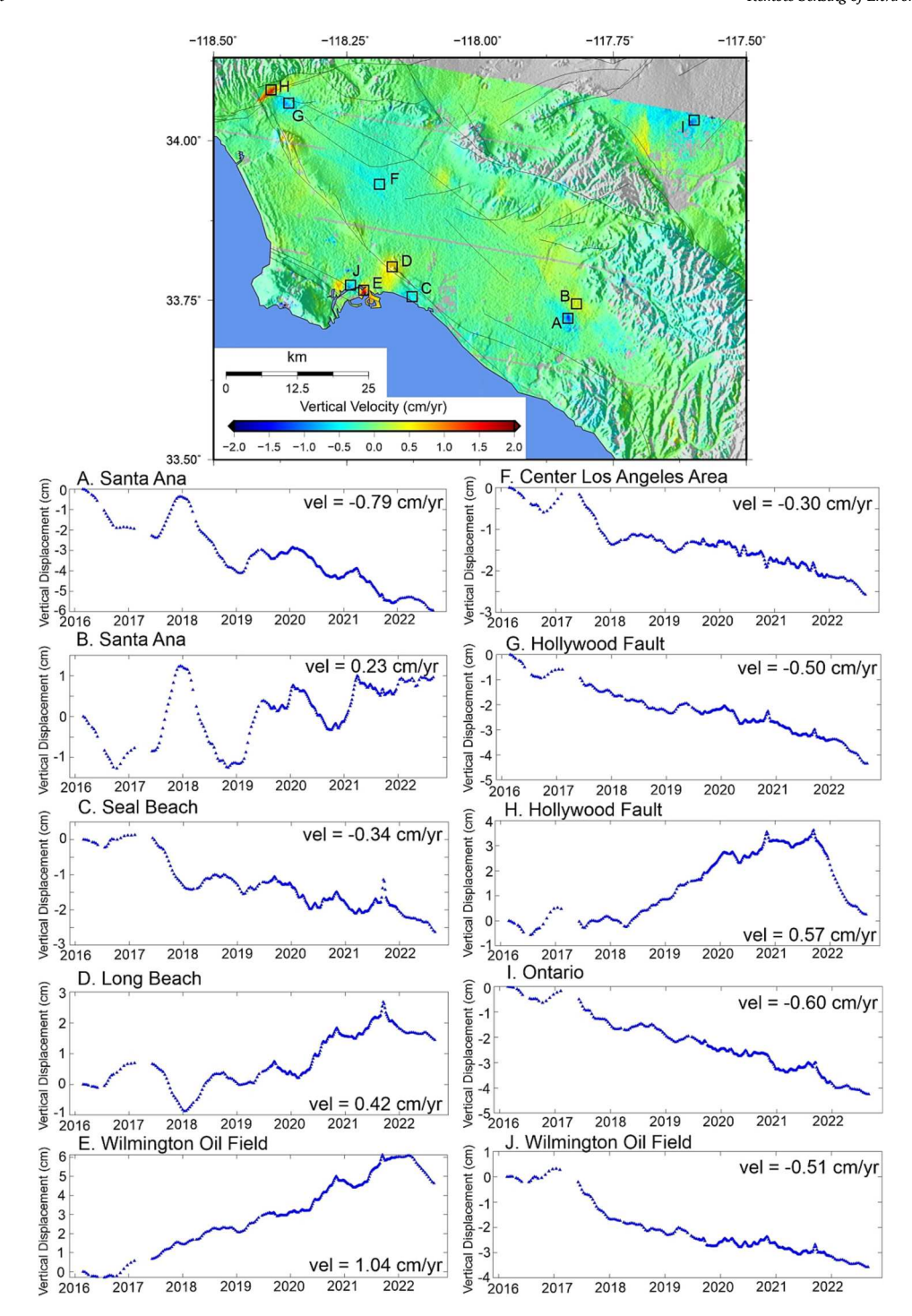


Fig. 15. Vertical land motion rate (top panel) across Los Angeles from 2016 to 2022 and selected vertical time series (lower panels). Here we apply a Gaussian filter of 18 days and a standard deviation of 0.3 cm to smooth each time series temporally.

measurements, our multitemporal SAR interferometric framework yields an accuracy of better than 0.5 cm and 0.3 cm for LOS displacement in rural and urban areas, respectively.

CRediT authorship contribution statement

Jui-Chi Lee: Conceptualization, Methodology, Software, Validation, Writing – original draft, Investigation, Visualization. **Manoochehr Shirzaei:** Conceptualization, Methodology, Software, Supervision, Writing – review & editing.

Declaration of Competing Interest

The authors declare the following financial interests/personal relationships which may be considered as potential competing interests:

Jui-Chi Lee reports financial support was provided by US National

Science Foundation. Manoochehr Shirzaei reports financial support was provided by US Department of Energy.

Data availability

Data will be made available on request.

References

- Ansari, H., de Zan, F., Bamler, R., 2018. Efficient phase estimation for interferogram stacks. IEEE Trans. Geosci. Remote Sens. 56 (7), 4109–4125. https://doi.org/ 10.1109/TGRS.2018.2826045.
- Ansari, H., de Zan, F., Parizzi, A., 2020. Study of systematic bias in measuring surface deformation with SAR interferometry. IEEE Trans. Geosci. Remote Sens. 1–1 https:// doi.org/10.1109/tgrs.2020.3003421.
- Bedford, J., Bevis, M., 2018. Greedy automatic signal decomposition and its application to daily GPS time series. J. Geophys. Res. Solid Earth 123 (8), 6992–7003. https://doi.org/10.1029/2017JB014765.
- Bekaert, D.P.S., Hooper, A., Wright, T.J., 2015. A spatially variable power law tropospheric correction technique for InSAR data. J. Geophys. Res. Solid Earth 2, 1–12. https://doi.org/10.1002/2014JB011557.A.
- Berardino, P., Fornaro, G., Lanari, R., Sansosti, E., 2002. A new algorithm for surface deformation monitoring based on small baseline differential SAR interferograms. IEEE Trans. Geosci. Remote Sens. 40 (11), 2375–2383. https://doi.org/10.1109/ TGRS.2002.803792.
- Blewitt, G., Hammoon, W.C., Kreener, C., 2018. Harnessing the GPS data explosion for interdisciplinary science. Eos 99. https://doi.org/10.1029/2018EO104623.
- Brooks, B.A., Merrifield, M.A., Foster, J., Werner, C.L., Gomez, F., Bevis, M., Gill, S., 2007. Space geodetic determination of spatial variability in relative sea level change, Los Angeles basin. Geophys. Res. Lett. 34 (1) https://doi.org/10.1029/2006GI.028171.
- Burgmann, R., Rosen, P.A., Fielding, E.J., 2000. Synthetic aperture radar interferometry to measure earth's surface topography and its deformation. Annu. Rev. Earth Planet. Sci. 28, 169–209. https://doi.org/10.1146/annurev.earth.28.1.169.
- Cao, N., Lee, H., Jung, H.C., 2016. A phase-decomposition-based PSInSAR processing method. IEEE Trans. Geosci. Remote Sens. 54 (2), 1074–1090. https://doi.org/ 10.1109/TGRS.2015.2473818.
- Cao, Y., Jónsson, S., Li, Z., 2021. Advanced InSAR tropospheric corrections from global atmospheric models that incorporate spatial stochastic properties of the troposphere. J.Geophys. Res. Solid Earth 126 (5), 1–20. https://doi.org/10.1029/2020JB020952.
- Costantini, M., 1998. A novel phase unwrapping method based on network programming. IEEE Trans. Geosci. Remote Sens. 36 (3), 813–821. https://doi.org/
- Costantini, M., Rosen, P.A., 1999. Generalized phase unwrapping approach for sparse data. In: International Geoscience and Remote Sensing Symposium (IGARSS), 1, pp. 267–269. https://doi.org/10.1109/igarss.1999.773467.
- de Boor, C., 1978. A Pratical Guid to Splines, Vol. 27. Springer-Verlag, New York.
- de Zan, F., Gomba, G., 2018. Vegetation and soil moisture inversion from SAR closure phases: first experiments and results. Remote Sens. Environ. 217 (March), 562–572. https://doi.org/10.1016/j.rse.2018.08.034.
- de Zan, F., Parizzi, A., Prats-Iraola, P., López-Dekker, P., 2014. A SAR interferometric model for soil moisture. IEEE Trans. Geosci. Remote Sens. 52 (1), 418–425. https://doi.org/10.1109/TGRS.2013.2241069.
- de Zan, F., Zonno, M., Lopez-Dekker, P., 2015. Phase inconsistencies and multiple scattering in SAR interferometry. IEEE Trans. Geosci. Remote Sens. 53 (12), 6608–6616. https://doi.org/10.1109/TGRS.2015.2444431.
- Dee, D.P., Uppala, S.M., Simmons, A.J., Berrisford, P., Poli, P., Kobayashi, S., Andrae, U., Balmaseda, M.A., Balsamo, G., Bauer, P., Bechtold, P., Beljaars, A.C.M., van de Berg, L., Bidlot, J., Bormann, N., Delsol, C., Dragani, R., Fuentes, M., Geer, A.J., Vitart, F., 2011. The ERA-interim reanalysis: configuration and performance of the data assimilation system. Q. J. R. Meteorol. Soc. 137 (656), 553–597. https://doi.org/10.1002/qj.828.
- Doin, M.P., Lasserre, C., Peltzer, G., Cavalié, O., Doubre, C., 2009. Corrections of stratified tropospheric delays in SAR interferometry: validation with global atmospheric models. J. Appl. Geophys. 69 (1), 35–50. https://doi.org/10.1016/j. jappgeo.2009.03.010.
- Duchon, J., 1977. In: Splines Minimizing Rotation-invariant Semi-norms in Sobolev Spaces, pp. 85–100. https://doi.org/10.1007/BFB0086566.
- Eff-Darwich, A., Pérez, J.C., Fernández, J., García-Lorenzo, B., González, A., González, P. J., 2012. Using a Mesoscale Meteorological Model to Reduce the Effect of Tropospheric Water Vapour from DInSAR Data: A Case Study for the Island of Tenerife, Canary Islands. Pure Appl. Geophys. 169 (8), 1425–1441. https://doi.org/10.1007/s00024-011-0401-4.
- Feng, J., Zhen, W., Wu, Z., 2017. Ionospheric effects on repeat-pass SAR interferometry. Adv. Space Res. 60 (7), 1504–1515. https://doi.org/10.1016/J.ASR.2017.06.019.
- Ferretti, A., Fumagalli, A., Novali, F., Prati, C., Rocca, F., Rucci, A., 2011. A new algorithm for processing interferometric data-stacks: SqueeSAR. IEEE Trans. Geosci. Remote Sens. 49 (9), 3460–3470. https://doi.org/10.1109/TGRS.2011.2124465.
- Ferretti, A., Prati, C., Rocca, F., 2001. Permanent scatterers in SAR interferometry. IEEE Trans. Geosci. Remote Sens. 39 (1), 8–20. https://doi.org/10.1109/36.898661.
- Fialko, Y., 2006. Interseismic strain accumulation and the earthquake potential on the southern San Andreas fault system. Nature 441 (7096), 968–971. https://doi.org/ 10.1038/nature04797.
- Fornaro, G., Verde, S., Reale, D., Pauciullo, A., 2015. CAESAR: an approach based on covariance matrix decomposition to improve multibaseline-multitemporal interferometric SAR processing. IEEE Trans. Geosci. Remote Sens. 53 (4), 2050–2065. https://doi.org/10.1109/TGRS.2014.2352853.
- Foster, J., Brooks, B., Cherubini, T., Shacat, C., Businger, S., Werner, C.L., 2006. Mitigating atmospheric noise for InSAR using a high resolution weather model. Geophys. Res. Lett. 33 (16), 1–5. https://doi.org/10.1029/2006GL026781.
- Foster, J., Kealy, J., Cherubini, T., Businger, S., Lu, Z., Murphy, M., 2013. The utility of atmospheric analyses for the mitigation of artifacts in InSAR. J. Geophys. Res. Solid Earth 118 (2), 748–758. https://doi.org/10.1002/jgrb.50093.

- Franceschetti, G., Lanari, R., 1999. Synthetic aperture radar processing. CRC Press. Goldfeld, S.M., Quandt, R.E., 1965. Some tests for homoscedasticity. J. Am. Stat. Assoc. 60 (310), 539–547.
- Gomba, G., Rodriguez Gonzalez, F., de Zan, F., 2017. Ionospheric phase screen compensation for the Sentinel-1 TOPS and ALOS-2 ScanSAR modes. IEEE Trans. Geosci. Remote Sens. 55 (1), 223–235. https://doi.org/10.1109/ TCPS. 2016.2604461
- Graham, R., Hell, P., 1985. On the history of the minimum spanning tree problem. Ann. Hist. Comput. 7 (1), 43–57.
- Gu, C., 2002. Smoothing Spline ANOVA Models. https://doi.org/10.1007/978-1-4757-3683-0.
- Guarnieri, A.M., Tebaldini, S., 2008. On the exploitation of target statistics for SAR interferometry applications. IEEE Trans. Geosci. Remote Sens. 46 (11), 3436–3443. https://doi.org/10.1109/TGRS.2008.2001756.
- Hanssen, R.F., 2001. Radar interferometry. In: Scientific American (Vol. 276, Issue 2). https://doi.org/10.1038/scientificamerican0297-46.
- Hobiger, T., Kinoshita, Y., Shimizu, S., Ichikawa, R., Furuya, M., Kondo, T., Koyama, Y., 2010. On the importance of accurately ray-traced troposphere corrections for interferometric SAR data. J. Geod. 84 (9), 537–546. https://doi.org/10.1007/s00190-010-0393-3.
- Hooper, A., 2008. A multi-temporal InSAR method incorporating both persistent scatterer and small baseline approaches. Geophys. Res. Lett. 35 (16), L16302. https://doi.org/10.1029/2008GL034654.
- Hooper, A., Segall, P., Zebker, H., 2007. Persistent scatterer interferometric synthetic aperture radar for crustal deformation analysis, with application to Volcán Alcedo, Galápagos. J. Geophys. Res. 112 (B7), B07407. https://doi.org/10.1029/ 2006JB004763.
- Lanari, R., Lundgren, P., Manzo, M., Casu, F., 2004. Satellite radar interferometry time series analysis of surface deformation for Los Angeles, California. Geophys. Res. Lett. 31 (23), 1–5. https://doi.org/10.1029/2004GL021294.
- Lee, J., Miller, A.R., Mango, S.A., 1994. Intensity and phase statistics of multilook polarimetric and interferometric SAR imagery. IEEE Trans. Geosci. Remote Sens. 32 (5), 1017–1028. https://doi.org/10.1109/36.312890.
- Li, Z., Fielding, E.J., Cross, P., Muller, J.-P., 2006. Interferometric synthetic aperture radar atmospheric correction: medium resolution imaging spectrometer and advanced synthetic aperture radar integration. Geophys. Res. Lett. 33 (6), L06816. https://doi.org/10.1029/2005GL025299.
- Li, Z., Fielding, E.J., Cross, P., Preusker, R., 2009. Advanced InSAR atmospheric correction: MERIS/MODIS combination and stacked water vapour models. Int. J. Remote Sens. 30 (13), 3343–3363. https://doi.org/10.1080/01431160802562172.
- Li, Z., Muller, J.-P., Cross, P., Fielding, E.J., 2005. Interferometric synthetic aperture radar (InSAR) atmospheric correction: GPS, moderate resolution imaging spectroradiometer (MODIS), and InSAR integration. J. Geophys. Res. 110 (B3), B03410. https://doi.org/10.1029/2004JB003446.
- Lin, Y.N.N., Simons, M., Hetland, E.A., Muse, P., Dicaprio, C., 2010. A multiscale approach to estimating topographically correlated propagation delays in radar interferograms. Geochem. Geophys. Geosyst. 11 (9), 1–17. https://doi.org/10.1029/ 2010GC003228
- Lindsey, E.O., Fialko, Y., 2013. Geodetic slip rates in the southern San Andreas fault system: effects of elastic heterogeneity and fault geometry. J. Geophys. Res. Solid Earth 118 (2), 689–697. https://doi.org/10.1029/2012/B009358.
- Löfgren, J.S., Björndahl, F., Moore, A.W., Webb, F.H., Fielding, E.J., Fishbein, E.F., 2010. Tropospheric correction for InSAR using interpolated ECMWF data and GPS zenith total delay from the Southern California integrated GPS network. Int. Geosci. Remote Sens. Symp. (IGARSS) 4503–4506. https://doi.org/10.1109/IGARSS.2010.5649888.
- Massonnet, D., Feigl, K.L., 1998. Radar interferometry and its application to changes in the Earth's surface. Rev. Geophys. 36 (4), 441–500. https://doi.org/10.1029/ 97RG03139
- Meyer, P.L., 1970. Introductory probability and statistical applications. Addison-Wesley Pub. Co., Reading, Mass.
- Michaelides, R.J., Zebker, H.A., Zheng, Y., 2019. An algorithm for estimating and correcting decorrelation phase from InSAR data using closure phase triplets. IEEE Trans. Geosci. Remote Sens. 57 (12), 10390–10397. https://doi.org/10.1109/ TGRS.2019.2934362.
- Mikhail, E.M., 1976. Observations and least squares. IEP.
- Onn, F., Zebker, H.A., 2006. Correction for interferometric synthetic aperture radar atmospheric phase artifacts using time series of zenith wet delay observations from a GPS network. J. Geophys. Res. 111 (B9), B09102. https://doi.org/10.1029/ 2005 B004012
- Pepe, A., 2009. Advanced differential interferometric SAR techniques: the extended minimum cost flow phase unwrapping (EMCF) technique. VDM publishing.
- Pepe, A., Lanari, R., 2006. On the extension of the minimum cost flow algorithm for phase unwrapping of multitemporal differential SAR interferograms. IEEE Trans. Geosci. Remote Sens. 44 (9), 2374–2383. https://doi.org/10.1109/ TGRS.2006.873207.
- Puysségur, B., Michel, R., Avouac, J.-P., 2007. Tropospheric phase delay in interferometric synthetic aperture radar estimated from meteorological model and multispectral imagery. J. Geophys. Res. 112 (B5), B05419. https://doi.org/10.1029/ 2006JB004352.
- Riel, B., Simons, M., Ponti, D., Agram, P., Jolivet, R., 2018. Quantifying ground deformation in the Los Angeles and Santa Ana coastal basins due to groundwater withdrawal. Water Resour. Res. 54 (5), 3557–3582. https://doi.org/10.1029/ 2017WD021078
- Rosen, P.A., Hensley, S., Joughin, I.R., Li, F.K., Madsen, S.N., Rodriguez, E., Goldstein, R. M., 2000. Synthetic aperture radar interferometry. Proc. IEEE 88 (3), 333–382. https://doi.org/10.1109/5.838084.

- Samsonov, S.V., Trishchenko, A.P., Tiampo, K., González, P.J., Zhang, Y., Fernández, J., 2014. Removal of systematic seasonal atmospheric signal from interferometric synthetic aperture radar ground deformation time series. Geophys. Res. Lett. 41 (17), 6123–6130. https://doi.org/10.1002/2014GL061307.
- Sansosti, E., Berardino, P., Manunta, M., Serafino, F., Fornaro, G., 2006. Geometrical SAR image registration. IEEE Trans. Geosci. Remote Sens. 44 (10), 2861–2870. https://doi.org/10.1109/TGRS.2006.875787.
- Schmidt, D.A., Bürgmann, R., 2003. Time-dependent land uplift and subsidence in the Santa Clara valley, California, from a large interferometric synthetic aperture radar data set. J. Geophys. Res. Solid Earth 108 (B9), 1–13. https://doi.org/10.1029/ 2002JB002267.
- Shanker, P., Casu, F., Zebker, H.A., Lanari, R., 2011. Comparison of persistent scatterers and small baseline time-series InSAR results: a case study of the San Francisco bay area. IEEE Geosci. Remote Sens. Lett. 8 (4), 592–596. https://doi.org/10.1109/ LGRS.2010.2095829.
- Shen, Z.K., Liu, Z., 2020. Integration of GPS and InSAR data for resolving 3-dimensional crustal deformation. Earth and space. Science 7 (4). https://doi.org/10.1029/
- Shirzaei, M., Bürgmann, R., 2012. Topography correlated atmospheric delay correction in radar interferometry using wavelet transforms. Geophys. Res. Lett. 39 (1), n/a-n/ a. https://doi.org/10.1029/2011GL049971.
- Shirzaei, M., Bürgmann, R., 2013. Time-dependent model of creep on the Hayward fault from joint inversion of 18 years of InSAR and surface creep data. J. Geophys. Res. Solid Earth 118 (4), 1733–1746. https://doi.org/10.1002/jgrb.50149.
- Shirzaei, M., Bürgmann, R., Fielding, E.J., 2017. Applicability of Sentinel-1 terrain observation by progressive scans multitemporal interferometry for monitoring slow ground motions in the San Francisco Bay Area. Geophys. Res. Lett. 44 (6), 2733–2742. https://doi.org/10.1002/2017GL072663.
- Shirzaei, M., Manga, M., Zhai, G., 2019. Hydraulic properties of injection formations constrained by surface deformation. Earth Planet. Sci. Lett. 515, 125–134. https://doi.org/10.1016/j.epsl.2019.03.025.
- Shirzaei, M., Walter, T.R., 2011. Estimating the effect of satellite orbital error using wavelet-based robust regression applied to InSAR deformation data. IEEE Trans. Geosci. Remote Sens. 49 (11), 4600–4605. https://doi.org/10.1109/ TGRS.2011.2143419.
- Tymofyeyeva, E., Fialko, Y., Jiang, J., Xu, X., Sandwell, D., Bilham, R., Rockwell, T.K., Blanton, C., Burkett, F., Gontz, A., Moafipoor, S., 2019. Slow slip event on the

- southern San Andreas fault triggered by the 2017 M w 8.2 Chiapas (Mexico) earthquake. J. Geophys. Res. Solid Earth 2018JB016765. https://doi.org/10.1029/2018JB016765.
- Wadge, G., Zhu, M., Holley, R.J., James, I.N., Clark, P.A., Wang, C., Woodage, M.J., 2010. Correction of atmospheric delay effects in radar interferometry using a nested mesoscale atmospheric model. J. Appl. Geophys. 72 (2), 141–149. https://doi.org/ 10.1016/j.jappgeo.2010.08.005.
- Walters, R.J., Elliott, J.R., Li, Z., Parsons, B., 2013. Rapid strain accumulation on the ashkabad fault (Turkmenistan) from atmosphere-corrected InSAR. J. Geophys. Res. Solid Earth 118 (7), 3674–3690. https://doi.org/10.1002/jgrb.50236.
- Webley, P.W., Wadge, G., James, I.N., 2004. Determining radio wave delay by non-hydrostatic atmospheric modelling of water vapour over mountains. Phys. Chem. Earth 29 (2–3), 139–148. https://doi.org/10.1016/j.pce.2004.01.013.
- Xu, X., Ward, L.A., Jiang, J., Smith-Konter, B., Tymofyeyeva, E., Lindsey, E.O., Sylvester, A.G., Sandwell, D.T., 2018. Surface creep rate of the southern San Andreas fault modulated by stress perturbations from nearby large events. Geophys. Res. Lett. 45 (19), 10259–10268. https://doi.org/10.1029/2018GL080137.
- Yague-Martinez, N., Prats-Iraola, P., Gonzalez, F.R., Brcic, R., Shau, R., Geudtner, D., Eineder, M., Bamler, R., 2016. Interferometric processing of Sentinel-1 TOPS data. IEEE Trans. Geosci. Remote Sens. 54 (4), 2220–2234. https://doi.org/10.1109/ TGRS.2015.2497902.
- Yu, C., Li, Z., Penna, N.T., 2018. Interferometric synthetic aperture radar atmospheric correction using a GPS-based iterative tropospheric decomposition model. Remote Sens. Environ. 204, 109–121. https://doi.org/10.1016/J.RSE.2017.10.038.
- Yu, C., Penna, N.T., Li, Z., 2017. Generation of real-time mode high-resolution water vapor fields from GPS observations. J. Geophys. Res. Atmos. 122 (3), 2008–2025. https://doi.org/10.1002/2016JD025753.
- Zebker, H.A., Villasenor, J., 1992. Decorrelation in interferometric radar echoes. IEEE Trans. Geosci. Remote Sens. 30 (5), 950–959. https://doi.org/10.1109/36.175330.
- Zhang, B., Zhu, W., Ding, X., Wang, C., Wu, S., Zhang, Q., 2022. A review of methods for mitigating ionospheric artifacts in differential SAR interferometry. Geodesy. Geodyn. 13 (2), 160–169. https://doi.org/10.1016/J.GEOG.2021.12.001.
- Zhang, Y., Fattahi, H., Amelung, F., 2019. Small baseline InSAR time series analysis: unwrapping error correction and noise reduction. Comput. Geosci. 104331 https://doi.org/10.1016/j.cageo.2019.104331.